Journal of Molecular Structure 1370 (2026) 146396

Contents lists available at ScienceDirect

Journal of Molecular Structure

journal homepage: www.elsevier.com/locate/molstr

Studying the cytotoxicity, molecular docking, and molecular dynamics of novel coumarin derivatives towards MCF-7 breast cancer cells

Aymen G. Faisel [a], Ali G. Swadi [b], Ahmed A. Majed [c,*], Amjed Abdulrasool [d], Tahseen A. Alsalim [c,*], Radwan Alanjjar [e], Aamal A. Al-Mutairi [f], Sami A. Al-Hussain [f], Magdi E.A. Zaki [f,*], Sobhi M. Gomha [g], Ahmed A. Elhenawy [h,i]

[a] Department of Applied Marine Sciences, College of Marine Sciences, University of Basrah, Basrah 61001, Iraq
[b] Department of Chemistry, Faculty of Pharmacy, University of Basrah, Basrah, Iraq
[c] Department of Chemistry, College of Education for Pure Sciences, University of Basrah, Basrah 61001, Iraq
[d] Department of Surgery, Kolding hospital, Sygehusvej 24, 6000 Kolding, Denmark
[e] CADD Unit, Faculty of Pharmacy, Libyan International Medical University, Benghazi, Libya
[f] Department of Chemistry, Faculty of Science, Imam Mohammad Ibn Saud Islamic University (IMSIU), Riyadh, Saudi Arabia
[g] Chemistry Department, Faculty of Science, Islamic University of Madinah, Madinah, 42351, Saudi Arabia
[h] Chemistry Department, Faculty of Science, Al-Baha University, Al-Baha 65731, Saudi Arabia
[i] Chemistry Department, Faculty of Science, Al-Azhar University, Cairo 11884, Egypt

ARTICLE INFO

Keywords:
Breast cancer
Coumarin
Triazole
Thiazolidinone
Molecular docking
MD

ABSTRACT

Breast cancer accounts for 2.3 million new cases annually, with acquired resistance limiting 5-fluorouracil (5-FU) efficacy. Coumarin-based hybrids have emerged as promising anticancer scaffolds due to their ability to interact with multiple biological targets. This study presents seven coumarin-heterocyclic hybrids (**6a-c, 7a-b, 8a-b**) synthesized via green sonochemistry (20 kHz, 60 °C) in 80–97% yields with 1–5 h reaction times, characterized by FT-IR, NMR, and MS. Cytotoxicity against MCF-7 cells identified thiazolidinone-coumarin **8b** as lead compound with IC_{50} = 26.4 ± 0.97 μg/mL, surpassing **5-FU** (IC_{50} = 98.58 ± 0.95 μg/mL) by 3.7-fold. Structure-activity relationships demonstrated, cyclization of hydrazone **7b** (IC_{50} = 61.1 μg/mL) to thiazolidinone **8b** improved potency 2.3-fold; the electron-donating substituents (4-OCH_3, 3,5-diOCH_3-4-OH) outperformed 4-CF_3 by 1.8–4.3-fold; while thiazolidinone ring closure consistently enhanced activity across series. Molecular docking against EGFR (PDB: 3RCD) identified **6a** as top binder with binding energy of −8.90 kcal/mol, establishing dual-anchor binding, hinge-region H-bonds with Val734 and π–π stacking with Phe1004. The molecular dynamic (MD) simulations validated superior **6a**-induced protein stabilization, RMSD 2.7 ± 0.3 Å versus 3.3 ± 0.4 Å for **8a,** reduced RMSF in flexible loops; 15% deeper pocket burial (MolSA), and 12% greater protein compaction (rGyr, SASA). The thiazolidinone-coumarin scaffold delivers exceptional anti-breast cancer activity validated by atomistic simulation. Structure-dynamic relationships from 200-ns MD provide rational guidance for next-generation kinase inhibitor design.

1. Introduction

Cancer is one of the leading causes of morbidity and mortality worldwide; for example, in 2020 breast cancer alone accounted for approximately 2.3 million new cases and 685,000 deaths annually [1]. The diversity of cancer types, the rise of drug resistance, and the off-target nature of traditional chemotherapy make the development of novel targeted anticancer drug compounds very necessary. Though there have been outstanding breakthroughs in therapeutic approaches within the last half-century, cancer continues to be a worldwide health burden, with mortality from the disease having little decline relative to major diseases [2–4]. Breast cancer is a leading cause of death in women from cancer globally among malignancies and annually millions of new breast cancer cases are diagnosed [5–7]. Breast cancer is heterogeneous and has been characterized by its expression of HR and HER2 and one such key model in HR-positive breast cancer is the MCF-7 cell line [8].

* Corresponding authors.
E-mail addresses: eduppg.ahmed.majed@uobasrah.edu.iq (A.A. Majed), tahseen.alsalim@uobasrah.edu.iq (T.A. Alsalim), magdizaki@ghmail.com (M.E.A. Zaki), ahmed.elhenawy@azhar.edu.eg (A.A. Elhenawy).

https://doi.org/10.1016/j.molstruc.2026.146396
Received 15 February 2026; Received in revised form 28 March 2026; Accepted 27 April 2026
Available online 27 April 2026

Given consistent and rising detection as an ongoing condition, the need to develop new, advanced therapeutic agents is more pressing than ever [9–12]. Heterocyclic compounds are known as privileged scaffolds in the field of drug discovery, due to their existence in a vast array of FDA-approved drugs and biologically active natural products [13–15]. Of these, the benzopyrone framework and coumarins, especially the coumarin (benzo-α-pyrone) scaffold, have been especially well known [16,17]. First isolated from Dipteryx odorata, coumarins and their derivatives like flavonoids exhibited a wide range of activities as pharmaceuticals, including antioxidant, anti-inflammatory, and antimicrobial active substances with potentialities [18–23]. Most importantly, the coumarin core has found its way to a favorable platform to develop anticancer agents as one of them [24–27]. It is shown to have properties such as induction of cell cycle arrest and activity against angiogenesis, which are two major benefits of these inhibitors. The planar character of the benzopyrone ring is believed to resemble the adenine complex of ATP, which makes the ketone capable of efficiently competing for an ATP-binding site of multiple protein kinases, one of the main promoters of oncogenesis [28]. Previous works have confirmed this belief confirming that certain coumarin derivatives may suppress the growth of breast cancer cell lines such as MCF-7 [29,30]. More interestingly, coumarin inhibitors are very helpful in anticancer activity on breast cancer. By lowering estrogen receptor alpha (ERα) expression and driving caspase-dependent apoptosis, it has been shown that 4-hydroxycoumarin inhibits MCF-7 cell proliferation [31]. More recent hybridized coumarin scaffolds have been found to have higher potency often exceeding clinical standards like 5-fluorouracil (5-FU) in vitro, for instance if the coumarin structure with triazoles and thiazolidinones were fused [32]. As an illustrative example of this, 5,7-diphenyloxy-4--methylcoumarin derivatives are highly effective against breast cancer cells because they block tubulin polymerization and VEGF signaling [31]. Given the favorable properties of the coumarin scaffold, it should be considered that molecular hybridization (covalently linking the privileged core to other pharmacologically active heterocyclic moieties) is a tested strategy for expanding its therapeutic uses. This approach might result in synergistic properties, enhanced binding affinity and new actions. With this in mind the focus was on identifying anticancer potential of new coumarin hybrids incorporating two established anticancer pharmacophores: the 1,2,4-triazole and thiazolidin-4-one ring systems [31,33]. Additionally, consistent with Green Chemistry principles, our main synthetic approach used ultrasound-assisted synthesis (sonochemistry). This contemporary approach exploits the effect of acoustic cavitation to produce localized high-energy hotspots and remarkably speeds up reaction rates as well as yields in mild, energy-efficient conditions [34,35].

This work, therefore, describes the efficient, green synthesis of a novel series of coumarin-triazole and coumarin-thiazolidinone hybrids. We then assessed their in vitro cytotoxic activity against the MCF-7 breast cancer cell line and employed a comprehensive in silico modeling approach to elucidate the molecular basis of their activity. Our findings reveal that these hybrid molecules, particularly the thiazolidinone derivatives, exhibit potent antiproliferative activity, identifying a promising new scaffold for the development of next-generation breast cancer therapeutics.

2. Material and methods

2.1. Instrumentation and spectral measurements

Merck, Sigma, and Fischer were the suppliers of the chemical ingredients and solvents. The IR spectra were collected by using Shemadzu FTIR spectrophotometer (model Affinity 1) in the region 4000–400 cm-1 in KBr disk. The mass spectra were scanned by the EI technique at 70 eV with an Agilent Technologies 5975 C spectrometer. The experimental values of ^{1}H and ^{13}C NMR spectra for the studied compounds were measured on a Bruker Advance (400 MHz and 100 MHz) spectrometer, TMS as the internal standard. DMSO-d_6 was used as a solvent.

2.2. Chemistry section

The synthesis of coumarin derivatives was carried out using ultrasound because, in contrast to traditional procedures, it can produce better yields and shorter reaction times.

2.2.1. Synthesis Procedure of 7-hydroxy-4-methyl-2H-chromen-2-one (1)

A mixture of ethyl acetoacetate (7 ml, 54 mmol), sulfuric acid (40 ml), and resorcinol (5 g, 46 mmol) were placed in a 100 mL sealed conical flask with a Teflon lid. Then, for four hours, the combination was exposed to 20 kHz ultrasound radiation at 60 °C. Through TLC, the reaction mixture was seen using EtOAc-hexane (4:6 v/v). Following the reaction's completion, the mixture was poured into 25 mL of cold water while being stirred, filtered, and the solid product was collected [36]. The mixture was then dissolved in 50 mL of 5% sodium hydroxide, acidified with a diluted solution of H_2SO_4, the coumarin product was collected and recrystallized from ethanol. White powder, Yield 97.62%, m.p.:190–188.5 °C. IR data (cm^{-1}): 3495, 3157, 3014, 2939, 1678, 1516,1452, 1390, 1274, 1068, 1124,1068,3495.

2.2.2. Synthesis Procedure of ethyl 2-((4-methyl-2-oxo-2H-chromen-7-yl) oxy) acetate (2)

Compound 1 (30 mmol, 5 g) was dissolved in 60 ml acetone in a conical flask with a stopper, potassium carbonate (55 mmol, 7.73 g), and 2-chloroethyl acetate (40 mmol, 4.9 g) were added to the reaction mixture. For three hours, the combination was exposed to 20 kHz ultrasound radiation. Through TLC, the reaction mixture was monitored using EtOAc-hexane (4:6 v/v). After the reaction is complete, the product is filtered and recrystallized from ethanol

White crystals, yield 80.64%. m.p.: 99–101 °C. IR data $(cm)^{-1}$: 3076,2978,1759,1710,1610 1558, 1425, 1389, 1269, 1197,1161,1085,1062, 842 [37].

2.2.3. Procedure for synthesis 2-((4-Methyl-2-oxo-2H-chromen-7-yl) oxy) acetohydrazide (3)

Compound 3 was synthesized by reacting compound **2** (20 mmol, 5 g) with hydrazine hydrate 80% (40 mmol, 1.88 g) in ethanol. The reaction vessel was exposed to 20 kHz ultrasound for 3 h after the reaction was complete, the solid product was filtered and recrystallized from ethanol. Light brown powder, Yield 97.87%, m.p.: 206–208 °C, IR data (υ, cm^{-1}): 3329, 3265, 3080, 2922,1728,1678,1610, 1525, 1440, 1267,1076,3329,3265.

2.2.4. Synthesis method of 7-((4-amino-5-thioxo-4,5-dihydro-1H-1,2,4-triazol-3-yl) methoxy)-4-methyl-2H-chromen-2-one. (5)

The first step is the synthesis of potassium 2-(2-((4-methyl-2-oxo-2H-chromen-7-yl) oxy) acetyl) hydrazine-1-carbodithioate compound (**4**), by adding compound (**3**) (4 g, 16 mmol) to the potassium hydroxide solution 30 ml (0.89 g, 16 mmol) then adding carbon sulfide (1.23 g, 16 mmol) to the reaction mixture, the reaction vessel was placed in the ultrasound device at 20 kHz ultrasound radiation at 60 °C for one hour, The light brown product was collected by filtering.

In the next step, compound 5 was synthesized from compound **(4)** (3 g, 8 mmol) that dissolved in ethanol (20 mL), and anhydrous hydrazine (0.75 mL) was added to the reaction vessel. The reaction combination was exposed to ultrasound at an approximate temperature of 60 °C and 20 kHz ultrasound radiation for two hours. Through TLC, the reaction mixture was monitored, and after the reaction was completely acidified with diluted hydrochloric acid, filtered, and recrystallized from dioxane. Yellow powder, Yield, 96%, m.p: 188–189 °C, IR data (υ, cm^{-1}); 3244, 3142, 3037, 2980, 1708, 1687, 1610, 1579, 1496, 1392, 1280, 1240, 1159, 1103, 1082, 966.

2.2.5. General Procedure for synthesis (6a-c)

Compounds **6a-c** were synthesized by dissolving compound **5** (0.5 g, 1.7 mmol) in 10 mL of dimethylformamide (DMF). The appropriate aldehyde (1.7 mmol) was added: 4-methoxybenzaldehyde for **6a**, 4-hydroxy-3,5-dimethoxybenzaldehyde for **6b**, and 4-methylthiobenzaldehyde for **6c**. *Para*-toluene sulfonic acid (0.07 g) was then added to the mixture. The reaction vessel was exposed to 20 kHz ultrasound radiation at temperature of 60 °C for 5 h, with reaction progress monitored by thin-layer chromatography (TLC). Upon completion, the mixture was poured into cold water, and the precipitated product was collected by filtration. The crude product was then recrystallized from ethanol/chloroform (6:4 v/v).

7-((6-(4-methoxyphenyl)-5,6-dihydro- [1,2,4] triazolo[3,4-b] [1,3,4] thiadiazol-3-yl) methoxy)-4-methyl-2H-chromen-2-one (6a)

IR (KBr, cm^{-1}): υ 3313 (N—H stretch), 3037 (aromatic C—H stretch), 2926 (aliphatic C—H stretch), 1685 (C=O stretch, lactone), 1604, 1510, 1420 (C=N, C=C stretches), 1301, 1251, 1168 (C—O-C stretch), 1028, 970, 835. **^{1}H NMR (400 MHz, DMSO-d6):** δ 11.56 (s, 1H, N—H), 8.01 (s, 1H, Ar-H), 7.82 (d, *J* = 8 Hz, 1H, Ar-H), 7.58 (d, *J* = 12 Hz, 1H, Ar-H), 7.23 (d, *J* = 8 Hz, 1H, Ar-H), 7.06 (d, *J* = 8 Hz, 1H, Ar-H), 6.25 (s, 1H, C═CH of coumarin), 5.28 (s, 1H, CH of thiadiazole ring), 4.79 (s, 2H, OCH_2), 3.83 (s, 3H, OCH_3), 2.40 (s, 3H, CH_3 of coumarin). **^{13}C NMR (100 MHz, DMSO-d6):** δ 165.3 (C=O, possibly thiadiazole or amide type carbonyl), 162.1 (C-7 of coumarin), 161.0 (C-2, coumarin lactone C=O), 158.9 (C-8a of coumarin), 142.7 (C-4 of coumarin), 130.4, 128.9, 128.7, 127 (Aromatic carbons of phenyl and coumarin rings), 114.8, 114.7, 114.5 (Aromatic CH carbons of coumarin and phenyl rings), 65.8 (OCH_2), 65.4 (CH of thiadiazole ring), 55.85 (OCH_3), 18.6 (CH_3 of coumarin). **MS (EI, 70 eV):** *m/z* 422.4 ([M]+), 161.1, 135.1, 121.1, 107.1, 77, 51.0.

7-((6-(4-hydroxy-3,5-dimethoxyphenyl)-5,6-dihydro- [1,2,4] triazolo[3,4-b] [1,3,4] thiadiazol-3-yl) methoxy)-4-methyl-2H-chromen-2-one (6b)

Light yellow powder. Yield, 84%, mp: 199–198 °C, **IR (KBr, cm^{-1}):** υ 3549 (O—H stretch), 3471 (N—H stretch), 3016 (aromatic C—H stretch), 2970 (aliphatic C—H stretch), 1668 (C=O stretch, lactone), 1600, 1514, 1460, 1423 (C=N, C=C stretches), 1344, 1309, 1224, 1128 (C—O-C stretch. **^{1}H NMR (400 MHz, DMSO-d6):** δ 11.38 (s, 1H, N—H), 9.06 (s, 1H, O—H), 7.68 (d, *J* = 4 Hz, 2H, Ar-H), 7.21 (s, 1H, Ar-H), 7.16 (s, 1H, Ar-H), 6.95 (d, *J* = 8 Hz, 2H, Ar-H), 6.22 (s, 1H, C═CH of coumarin), 5.32 (s, 1H, CH of thiadiazole ring), 4.77 (s, 2H, OCH_2), 3.83 (s, 6H, OCH_3), 2.39 (s, 3H, CH_3 of coumarin). **^{13}C NMR (100 MHz, DMSO-d6):** δ 170.2 (C = O, possibly thiadiazole or amide type carbonyl), 161.4 (C-7 of coumarin), 160.6 (C-2, coumarin lactone C = O), 155.0, 153.8 (C-4a, coumarin; quaternary carbons of dimethoxyphenyl ring), 148.5 (C-4 of coumarin), 139.3, 128.5, 127.5, 126.9, 125.9, 124.7 (Aromatic carbons of dimethoxyphenyl and coumarin rings), 113.8 (C-3 of coumarin), 112.7, 111.7, 106.2, 101.9 (Aromatic CH carbons of coumarin and dimethoxyphenyl), 66.6 (OCH_2), 65.7 (CH of thiadiazole ring), 56.4 (OCH_3), 18.6 (CH_3 of coumarin). **MS (EI, 70 eV):** *m/z* 468.5 ([M]+), 360.01, 147.1, 123.1, 51.0.

4-methyl-7-((6-(4-(Methylthio) phenyl)-5,6-dihydro- [1,2,4] triazolo[3,4-b] [1,3,4] thiadiazol-3-yl) methoxy)-2H-chromen-2-one (6c)

Yellow powder. Yield 83%, mp:180–181 °C, **IR (KBr, cm^{-1}):** υ 3462 (N—H stretch), 3047 (aromatic C—H stretch), 2976 (aliphatic C—H stretch), 1689 (C = O stretch, lactone), 1622, 1593, 1552, 1490, 1404 (C = N, C = C stretches), 1315, 1182, 1089 (C—O-C stretch). **^{1}H NMR (400 MHz, DMSO-d6):** δ 11.65 (s, 1H, N—H), 7.80 (d, *J* = 8 Hz, 1H, Ar-H), 7.69 (d, *J* = 8 Hz, 2H, Ar-H), 7.36 (d, *J* = 8 Hz, 1H, Ar-H), 6.96 (t, *J* = 12 Hz, 1H, Ar-H), 6.24 (s, 1H, C═CH of coumarin), 5.29 (s, 1H, CH of thiadiazole ring), 4.80 (s, 2H, OCH_2), 2.54 (s, 3H, SCH_3), 2.40 (s, 3H, CH_3 of coumarin). **^{13}C NMR (100 MHz, DMSO-d6):** δ 170.1 (C═O, possibly thiadiazole or amide type carbonyl), 161.5, 161.4 (C-7 of coumarin; C-2, coumarin lactone C═O), 153.8 (C-4a of coumarin), 143.3 (C-4 of coumarin), 130.6, 129.1, 128, 127.8, 127.6, 126.9, 126, 125.9 (Aromatic carbons of methylthiophenyl and coumarin rings), 113.9 (C-3 of coumarin), 112.8, 111.7, 102, 101.9 (Aromatic CH carbons of coumarin), 66 (OCH_2), 65.4 (CH of thiadiazole ring), 18.6 (CH_3 of coumarin), 14.7 (SCH_3). **MS (EI, 70 eV):** *m/z* 438.1 ([M]+), 316.1, 300.1, 248.1, 147.1, 77, 50.1.

2.2.6. General method for synthesis (7a, 7b)

Compound **3** (0.5 g, 2mmole) was dissolved in 20 mL of absolute ethanol, appropriate aldehyde (2mmole) was added to the reaction mixture with a few drops of glacial acetic acid, the vessel of the was exposed to ultrasound at an approximate temperature of 60 °C and 20 kHz ultrasound radiation for 2 h. The reaction product filtered and recrystallized from ethanol.

N'-(4-hydroxy-3,5-dimethoxybenzylidene)-2-((4-methyl-2-oxo-2H-chromen-7-yl)oxy)acetohydrazide (7a)

White powder Yield 86.41%, mp: 223–224 °C, **IR (KBr, cm^{-1}):** υ 3392 (O—H stretch), 3076 (aromatic C—H stretch), 2995 (aliphatic C—H stretch), 1718 (C=O stretch, lactone), 1689 (C=O stretch, hydrazide), 1618 (C=N stretch, azomethine), 1435, 1409 (C=C stretches), 1327, 1276, 1199, 1157, 1112, 1066, 977, 844. **^{1}H NMR (400 MHz, DMSO-d6):** δ 11.87 (s, 1H, N—H), 8.40 (s, 1H, CH═N), 8.09–7.68 (m, 4H, Ar-H), 7.0 (d, 2H, Ar-H), 6.22 (s, 1H, C═CH of coumarin), 4.85 (s, 2H, OCH_2), 2.39 (s, 3H, CH_3 of coumarin). **^{13}C NMR (100 MHz, DMSO-d6):** δ 169.2 (C=O, hydrazide), 166.5 (C=O, lactone), 164.4 (CH=N, azomethine carbon), 161.7 (C-7 of coumarin), 160.5 (C-2, coumarin lactone C=O), 155 (C-4a of coumarin), 153.8 (quaternary carbons of dimethoxyphenyl), 142.7 (C-4 of coumarin), 128.2, 127, 126.8, 125.9 (Aromatic carbons of dimethoxyphenyl and coumarin rings), 123.2, 113.8 (C-3 of coumarin), 112.9, 111.7, 102.1 (Aromatic CH carbons of coumarin), 65.6 (OCH_2), 18.6 (CH_3 of coumarin). **MS (EI, 70 eV):** *m/z* 404.2 ([M]+), 229.1, 189.1, 176.1, 161.1, 148.1, 131.1, 118.1, 77.1, 51.0.

N'-(4-hydroxy-3,5-dimethoxybenzylidene)-2-((4-methyl-2-oxo-2H-chromen-7-yl)oxy)acetohydrazide (7b)

White powder, Yield 85%, mp: 223–224 °C, **IR (KBr, cm^{-1}):** υ 3508 (N—H stretch), 3311 (O—H stretch, *likely a typo, compound 7b has CF_3 not OH*), 3076 (aromatic C—H stretch), 2995 (aliphatic C—H stretch), 1710 (C=O stretch, lactone), 1670 (C=O stretch, hydrazide), 1625 (C=N stretch, azomethine), 1597, 1552, 1517, 1460, 1427 (C=C stretches), 1388, 1336, 1294, 1226, 1153, 1120, 1080, 956, 335. **^{1}H NMR (400 MHz, DMSO-d6):** δ 11.58 (s, 1H, N—H), 8.93 (b, 1H, *OH*), 8.20 (s, 1H, CH═N), 7.90–7.65 (m, 4H, Ar-H), 6.97 (t, *J* = 12 Hz, 1H, Ar-H), 6.19 (s, 1H, C═CH of coumarin), 4.80 (s, 2H, OCH_2), 3.89 (s, 6H, OCH_3), 2.38 (s, 3H, CH_3 of coumarin). **^{13}C NMR (100 MHz, DMSO-d6):** δ 168.7 (C=O, hydrazide), 163.7 (CH═N, azomethine carbon), 161.8 (C-7 of coumarin), 160.5 (C-2, coumarin lactone C═O), 154.9 (C-4a of coumarin), 148.5 (C-4 of coumarin), 138.5, 126.8, 124.6 (Aromatic carbons), 114.1 (C-3 of coumarin), 112.8, 111.6, 105.2, 102 (Aromatic CH carbons of coumarin), 65.7 (OCH_2), 53.8 (OCH_3), 18.5 (CH_3 of coumarin). **MS (EI, 70 eV):** *m/z* 412.2 ([M]+), 233.1, 189.1, 176.1, 118.1, 103.1, 77.

2.2.7. General Procedure for synthesis (8a, 8b)

Compound (**7b**) or (**7a**) (1 mmol) was dissolved in 10 ml of dioxane. The thioglycolic acid (0.11 g, 1 mmol) and zinc chloride (0.2 g) were added to the reaction mixture. The reaction was exposed to ultrasound at 20 kHz ultrasound radiation for 3 h, and the reaction product was filtered and recrystallized from ethanol.

2-((4-methyl-2-oxo-2H-chromen-7-yl) oxy)-N-(4-oxo-2-(4-(trifluoromethyl) phenyl) thiazolidin-3-yl) acetamide (8a) white powder: Yield 85%, mp: 215–217 °C, **IR (KBr, cm^{-1}):** υ 3414 (N—H stretch), 3205 (aromatic C—H stretch), 3082 (aromatic C—H stretch), 2968 (aliphatic C—H stretch), 1722 (C=O stretch, lactone), 1689 (C=O stretch, amide), 1614 (C=O stretch, thiazolidinone), 1558, 1510, 1408, 1392 (C=N, C=C stretches). **^{1}H NMR (400 MHz, DMSO-d6):** δ 11.86 (s, 1H, N—H), 8.10–7.71 (m, 4H, Ar-H), 7.08–7.00 (m, 2H, Ar-H), 6.23 (s,

1H, C═CH of coumarin), 5.34 (s, 1H, CH of thiazolidinone), 4.85 (s, 2H, OCH_2), 2.41 (s, 3H, CH_3 of coumarin). **^{13}C NMR (100 MHz, DMSO-d6):** δ 169.2 (C═O, acetamide), 164.4 (C-4, thiazolidinone C═O), 161.7 (C-2, coumarin lactone C═O), 160.5 (C-7 of coumarin), 155.0 (C-4a of coumarin), 153.8 (C-8a of coumarin), 146.7 (quaternary carbon of trifluoromethylphenyl), 142.7 (C-4 of coumarin), 138.3 (quaternary carbon of trifluoromethylphenyl), 128.2, 126.8, 126.1 (Aromatic carbons of trifluoromethylphenyl and coumarin rings), 113.8 (C-3 of coumarin), 112.9, 111.7, 102 (Aromatic CH carbons of coumarin), 67 (CH of thiazolidinone), 65.6 (OCH_2), 18.6 (CH_3 of coumarin). **MS (EI, 70 eV):** *m/z* 478.5 ([M]+), 175.1, 148.2, 131.1, 117.1, 103.1, 77.0, 51.0.

N-(2-(4-hydroxy-3,5-dimethoxyphenyl)-4-oxothiazolidin-3-yl)-2-((4-methyl-2-oxo-2H-chromen-7-yl) oxy) acetamide (8b) yellow powder, Yield 86%, mp : 215–217 °C, **IR (KBr, cm^{-1}):** 4441, 3221 (O—H stretch), 3089 (aromatic C—H stretch), 2970 (aliphatic C—H stretch), 1716 (C═O stretch, lactone), 1697 (C═O stretch, amide), 1612 (C═O stretch, thiazolidinone), 1560, 1512, 1427, 1392 (C═N, C═C stretches). **^{1}H NMR (400 MHz, DMSO-d6):** δ 11.58 (s, 1H, N—H), 8.96 (s, 1H, O—H), 8.19–7.68 (m, 2H, Ar-H), 7.06–6.95 (m, 2H, Ar-H), 6.22 (s, 1H, C═CH of coumarin), 5.32 (s, 1H, CH of thiazolidinone), 4.80 (s, 2H, OCH_2), 3.98–4.06 (dd, 2H, CH_2-S of thiazolidinone), 3.81 (s, 6H, OCH_3), 2.40 (s, 3H, CH_3 of coumarin). **^{13}C NMR (100 MHz, DMSO-d6):** δ 168.7 (C═O, acetamide), 163.7 (C-4, thiazolidinone C═O), 161.9 (C-2, coumarin lactone C═O), 160.6 (C-7 of coumarin), 155 (C-4a of coumarin), 153.9 (C-8a of coumarin), 148.5 (C-4 of coumarin; quaternary carbons of dimethoxyphenyl), 138.2 (quaternary carbon of dimethoxyphenyl), 126.8, 124.6 (Aromatic carbons of dimethoxyphenyl and coumarin rings), 113.7 (C-3 of coumarin), 112.9, 111.6, 105, 102 (Aromatic CH carbons of coumarin and dimethoxyphenyl), 67 (CH of thiazolidinone), 65.7 (OCH_2), 56.4 (OCH_3), 30.9 (CH_2S of thiazolidinone), 18.6 (CH_3 of coumarin). **MS (EI, 70 eV):** *m/z* 486.5 ([M]+), 414.41, 176.1, 148.1, 103.1, 77.1, 51.1.

2.3. MTT cell viability assay

The cytotoxic effects of the designed coumarin derivatives on MCF-7 human breast cancer cells were compared by the MTT [3-(4,5-dimethylthiazol-2-yl)-2,5-diphenyltetrazolium bromide (Sigma-Aldrich)] assay as described in previous [38,39]. The MCF-7 human breast adenocarcinoma cell line was obtained from the American Type Culture Collection (ATCC, Manassas, VA, USA; catalog number HTB-22™**).** Cells were cultured in Dulbecco's Modified Eagle Medium (DMEM, Gibco, Thermo Fisher Scientific, Waltham, MA, USA) supplemented with 10% fetal bovine serum (FBS, Gibco), 100 U/mL penicillin, and 100 μg/mL streptomycin (Sigma-Aldrich, St. Louis, MO, USA) at 37 °C in a humidified atmosphere containing 5% CO_2.

To ensure comparable metabolic activity measurements, MCF-7 breast cancer cells were cultured in 96-well plates at a density of 1×10^4 cells/well. Plates were prepared with a final volume of 100 μL/well for standardization of conditions. Cells were treated with six concentrations of the synthesized coumarin derivatives: 7.5 μM, 22 μM, 66 μM, 200 μM, and 600 μM to establish dose-response relationships and calculate IC_{50} values. 5-Fluorouracil was used as a reference cytotoxic agent for comparison MTT solution (3-(4,5-dimethylthiazol-2-yl)-2,5-diphenyltetrazolium bromide) was prepared in serum-free media and added to each well at 50 μL/well. Plates were incubated at 37 °C for 2–4 h to allow mitochondrial reduction of MTT to purple formazan crystals. After incubation, the MTT solution was removed, and 100 μL of MTT solvent. The half-maximal inhibitory concentration (IC_{50}) was calculated by non-linear regression analysis using dose-response curves plotted as percentage cell viability versus log compound concentration. Python software (version 3.14.3) was used for all calculations.

2.4. Computational model

All computational modeling, including molecular docking and molecular dynamics simulations, was performed using the Schrödinger Maestro Molecular Modeling Suite (Version 2023–1, Schrödinger, LLC, New York, NY, USA) on a high-performance computing cluster [40]. The OPLS4 force field was employed for all energy calculations and minimizations, ensuring a consistent and accurate representation of the system's energetics.

2.4.1. Protein Preparation and active site definition

To ensure a biologically relevant and computationally ready model of the target, the high-resolution crystal structure of the human EGFR kinase domain (PDB ID: **3RCD**) was prepared using the Protein Preparation Wizard in Maestro. Protonation and tautomeric states for all residues, at a physiological pH of 7.4 ± 0.5 using PROPKA, removal of all water molecules beyond 5 Å of the co-crystallized ligand to retain key hydrating waters. Finally, the entire protein structure was subjected to a restrained energy minimization using the OPLS4 force field, converging when the root-mean-square deviation (RMSD) of heavy atoms reached a threshold of 0.30 Å. This crucial step relieves any steric clashes present in the static crystal structure and optimizes the hydrogen-bonding network.

2.4.2. Ligand Preparation

The 2D structures of all synthesized compounds (**6a-c, 7a-b, 8a-b**) and the reference inhibitor were prepared for docking using the **LigPrep** module. This workflow is essential for generating accurate, low-energy, 3D conformations, through generation of possible ionization states at the target physiological pH of 7.4 ± 0.5 using Epik. Then, generation of stereoisomers and tautomers where applicable. The energy minimization of each generated conformer using the OPLS4 force field to produce a library of realistic, low-energy structures for each ligand.

2.4.3. Molecular Docking

The active site was first defined through building a receptor grid using the Receptor Grid Generation tool before docking. Molecular docking was accomplished by means of the Glide (Grid-based Ligand Docking with Energetics) module. An Extra Precision (XP) mode was used to facilitate the highest accuracy. The prepared ligands were then flexibly docked through the rigid receptor grid. The final scoring was carried out on the GlideScore XP function, which enables a more sophisticated treatment of solvation, hydrophobic interactions, and penalties for steric clashes. For each ligand, the top ten scoring poses in this process were saved, and the pose with the best GlideScore (being the most negative) was the one chosen for further analysis and subsequent MD simulations..

2.4.4. Molecular Dynamics (MD) simulation protocol

To validate the stability of the top-ranked docking poses and to explore the dynamic behavior of the protein-ligand complexes, all-atom MD simulations were performed for 200 nanoseconds (ns) using the Desmond module. The highest-scoring docked complex of each ligand with EGFR was used as the starting structure. Each complex was solvated in an orthorhombic box using the TIP3P explicit water model, with a buffer distance of 10 Å from the protein surface to the box edges. The system was neutralized by adding an appropriate number of Na^+ or Cl^- counter-ions. To relax the system and prepare it for the production run, a default multi-stage equilibration protocol was applied. This protocol consists of a series of restrained minimizations and short MD simulations under NVT (constant volume) and NPT (constant pressure) ensembles to gradually heat the system to 300 K and adjust the solvent density, while allowing the protein and ligand to relax in the explicit solvent environment. The equilibrated systems were subjected to a 200 ns production run in the NPT ensemble. The temperature was maintained at 300 K using the Nosé-Hoover chain thermostat, and the pressure was maintained at 1.01325 bar using the Martyna-Tobias-Klein barostat. The integration time step was set to 2.0 fs, and the SHAKE algorithm was applied to constrain all bonds involving hydrogen atoms. The OPLS4

force field was used for all atoms. Trajectory snapshots were saved every 200 ps for subsequent analysis.

2.5. Statistical analysis

All biological experiments were performed in triplicate, and data are expressed as mean ± standard deviation (SD). IC_{50} values were calculated using non-linear regression analysis (variable slope, four-parameter logistic curve) in Python software (version 3.14.3). Statistical comparisons between treatment groups and control were performed using one-way analysis of variance (ANOVA) followed by Dunnett's post-hoc test. Differences were considered statistically significant at $p^* < 0.05$. For computational analyses, RMSD, RMSF, rGyr, SASA, and MolSA values were calculated as mean ± SD over the 200 ns simulation trajectory after equilibration.

2.6. Safety assessment and limitations

In silico safety profiling was performed to assess the therapeutic window of lead compounds. ADMET (Absorption, Distribution, Metabolism, Excretion, and Toxicity) properties were predicted using the ADMETlab 2 web server. Parameters including human intestinal absorption (HIA), blood-brain barrier (BBB) permeability, CYP450 inhibition, AMES toxicity, and hERG channel inhibition were evaluated for compounds **6a, 8a**, and **8b**

3. Results and discussion

3.1. Chemistry

3.1.1. Step-by-Step Analysis of the sonochemical pathway

Under Scheme 1 to 3 synthetic strategies present a modern, effective method for organic synthesis focused on ultrasound irradiation (20 kHz). As an essential step of sonochemistry, this procedure is employed intentionally to increase reaction rates, improve yields, and operate under milder conditions, in accordance with the fundamental premises of Green Chemistry. Ultrasound-assisted synthesis does not rely on direct molecular interaction with sound waves. Instead, its power stems from acoustic cavitation: the formation, growth, and violent implosive collapse of microscopic bubbles in the liquid medium. The collapse of these cavities generates transient, localized (hotspots) with extreme conditions (~5000 K, ~1000 atm), shockwaves, and high-speed microjets. These effects are responsible for the observed chemical enhancements by providing, enhanced mass transfer, surface activation, and high-energy input, The hotspots provide an immense amount of localized energy to overcome activation energy barriers.

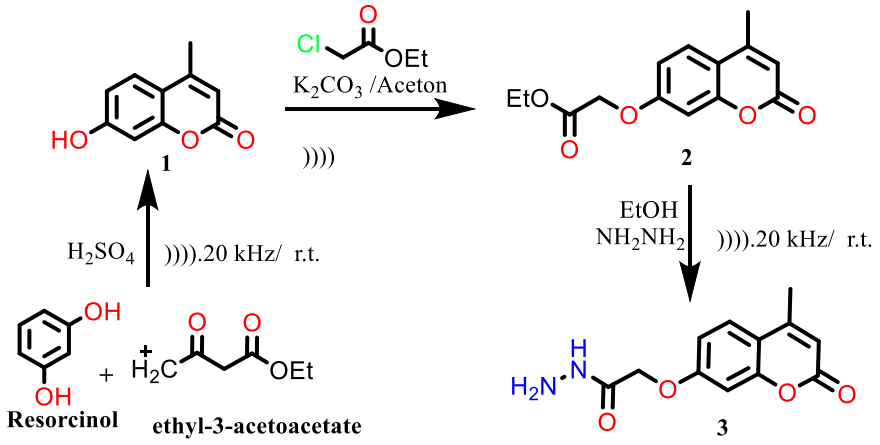

Scheme 1. Specific Synthetic Steps for synthesis of compounds 2, and 3 using Ultrasound at 20 kHz at r. t. C.

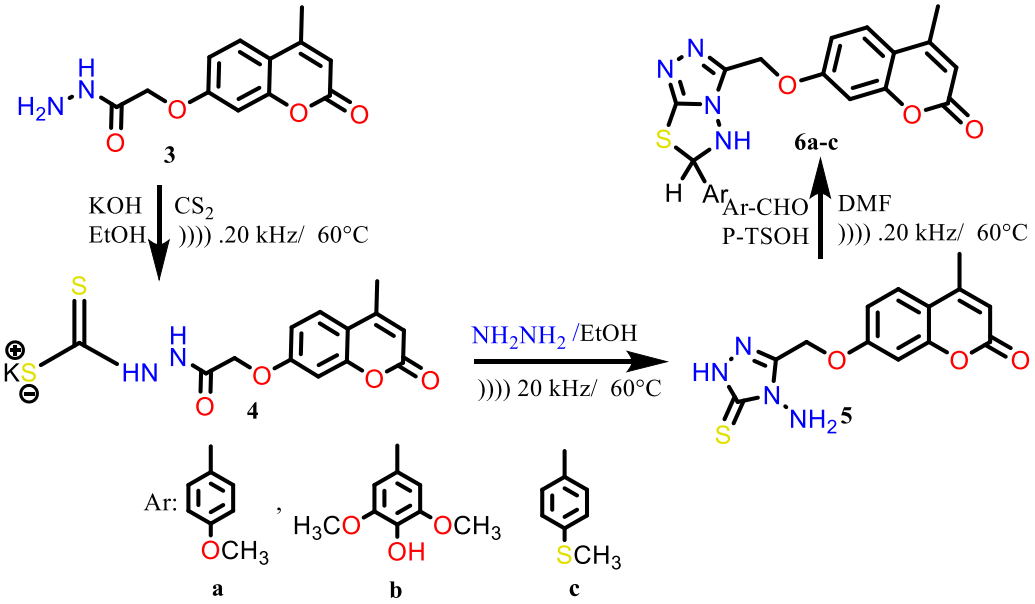

Scheme 2. Synthetic Steps for synthesis of compounds 5, and 6a-c by applying ultrasound at 20 kHz at 60 °C.

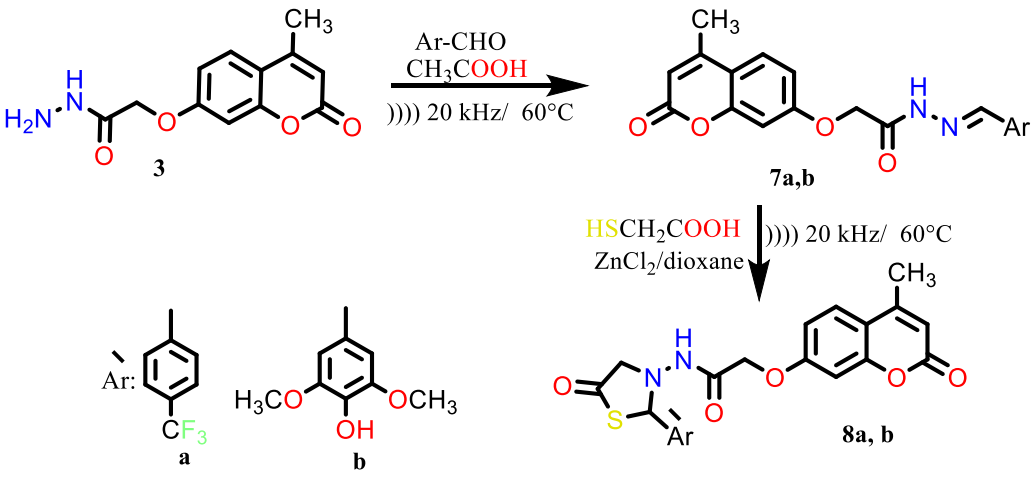

Scheme 3. Synthetic Steps for synthesis of compounds 7, and 8 by applying Ultrasound at 20 kHz at 60 °C.

Firstly, Pechmann Condensation used to synthesis of the coumarin core **1** from resorcinol and ethyl-3-acetoacetate is catalyzed by concentrated H_2SO_4. This is a highly viscous medium where conventional stirring is often inefficient. Ultrasound irradiation excels here by providing powerful, uniform mixing that overcomes the high viscosity. The cavitation hotspots supply the necessary localized energy to drive both the initial transesterification and the subsequent intramolecular cyclization/dehydration, all while the bulk temperature remains at room temperature (r.t.). This results in a remarkably high yield (97.62%) in a fraction of the time required for traditional thermal methods. Williamson Ether Synthesis used to Formation. This step involves the reaction of coumarin **1** with ethyl 2-chloroacetate in the presence of K_2CO_3. This is a classic heterogeneous solid-liquid phase reaction, where the rate is typically limited by the surface area of the solid base. Ultrasound irradiation provides a profound advantage. The microjets and shockwaves generated by cavitation continuously bombard the K_2CO_3 particles. This sonomechanical effect de-agglomerates the solid, reduces particle size, and scours the surface clean of any passivating layers, thus maximizing the reactive interface. That accelerates S_N2 displacement by disrupting H-bonding networks around phenolic OH. The result is a rapid and efficient S_N2 reaction, completed in just three hours with a high yield 80.64% (vs. 65% conventional) with minimized diester biproducts. The conversion of ester **2** to the pivotal hydrazide intermediate **3** is a nucleophilic acyl substitution. While this is a homogeneous reaction, it still benefits significantly from sonication. The intense micro-mixing ensures that the hydrazine hydrate and ester molecules are constantly brought into contact, increasing the frequency of effective collisions. The high-energy hotspots can facilitate the formation of the tetrahedral intermediate, accelerating the overall reaction rate and leading to a near-quantitative yield (97.87%) in a short timeframe Scheme 1.

The sequence in Scheme-2 starts with the reaction of hydrazide **3** with CS_2 and KOH to prepare the potassium dithiocarbazate salt 4. The intramolecular cyclocondensation resulting from the addition of hydrazine hydrate results in an elimination of H_2S for the final formation of the 4-amino-5-thioxo-1,2,4-triazole **5**. The elimination of H_2S acts as an important energy barrier. The cavitation hotspots provide the requisite localized energy to drive the elimination efficiently, pushing the equilibrium towards the cyclized product. The entire process is accomplished in a mere two hours with an excellent 96% yield which strongly demonstrates the effectiveness of the sonochemical method. Final cyclocondensation step to formation of **6a-c**.This final step involves the reaction of triazole **5** with various aromatic aldehydes (Ar-CHO) to form the fused triazolo[3,4-b] [1,3,4]thiadiazole ring system. This is a multi-stage process involving the formation of a Schiff base intermediate, followed by an intramolecular nucleophilic attack and dehydration. Such condensation reactions typically require heat and azeotropic removal of water. Ultrasound provides a superior alternative. The localized hotspots supply the activation energy for both the initial imine formation and the final ring-closing dehydration, catalyzed by p-TSOH. This occurs efficiently at a controlled bulk temperature of 60 °C, which is mild enough to prevent thermal degradation of the complex heterocyclic products, resulting in clean reactions and excellent yields (83–87%) in only five hours (Fig. 1).

The final fused-ring system is constructed by reacting the triazole **5** with various substituted aromatic aldehydes. This is a cyclocondensation reaction where the exocyclic amino group of the triazole condenses with the aldehyde to form a Schiff base intermediate (not isolated), which then undergoes an intramolecular cyclization via nucleophilic attack of the ring's sulfur atom onto the imine carbon. Subsequent dehydration, catalyzed by p-toluenesulfonic acid (p-TSOH), yields the target 5,6-dihydro- [1,2,4]triazolo[3,4-b] [1,3,4]thiadiazole derivatives (**6a-c**). **Pathway B:** Synthesis of the Thiazolidin-4-one Series **(8a, b).** The hydrazide **3** is condensed with appropriate aromatic aldehydes in the presence of a catalytic amount of glacial acetic acid. The terminal -NH_2 group of the hydrazide acts as a nucleophile, attacking the aldehyde's carbonyl carbon, followed by dehydration to form the corresponding N-acylhydrazone derivatives (Schiff bases) **7a** and **7b** The thiazolidin-4-one ring is formed via a cyclocondensation reaction between the Schiff bases (**7a, 7b**) and thioglycolic acid ($HSCH_2COOH$). In this reaction, the thiol group of thioglycolic acid adds across the C=N double bond of the Schiff base. This is followed by an intramolecular cyclization where the nitrogen atom attacks the carboxylic acid's carbonyl group, leading to the elimination of a water molecule and the formation of the five-membered thiazolidin-4-one ring. Zinc chloride ($ZnCl_2$) likely acts as a Lewis acid catalyst to activate the imine bond towards nucleophilic attack.

The repeatable application of ultrasound in our syntheses demonstrates both a straightforward and effective approach with numerous advantages. Fast reaction; reaction times are low overall (3–5 h) in comparison to classic heat treatment techniques with a time frame for a comparable transformation of 8–24 h (Table 1). High Yields: The produced yields are reliably very high (generally, over 85–95%), denoting highly efficient conversions and minimal side-product formation (Table S-1). Energy Efficiency and Mild Conditions, all of the reactions are performed at a low bulk temperature of 60 °C, hence the procedure is energy efficient and avoids the possibility of thermal decomposition of the complex heterocyclic products. This is a foundational principle of green chemistry.

3.1.2. Spectroscopic Structural elucidation

The structural integrity of the synthesized compounds was

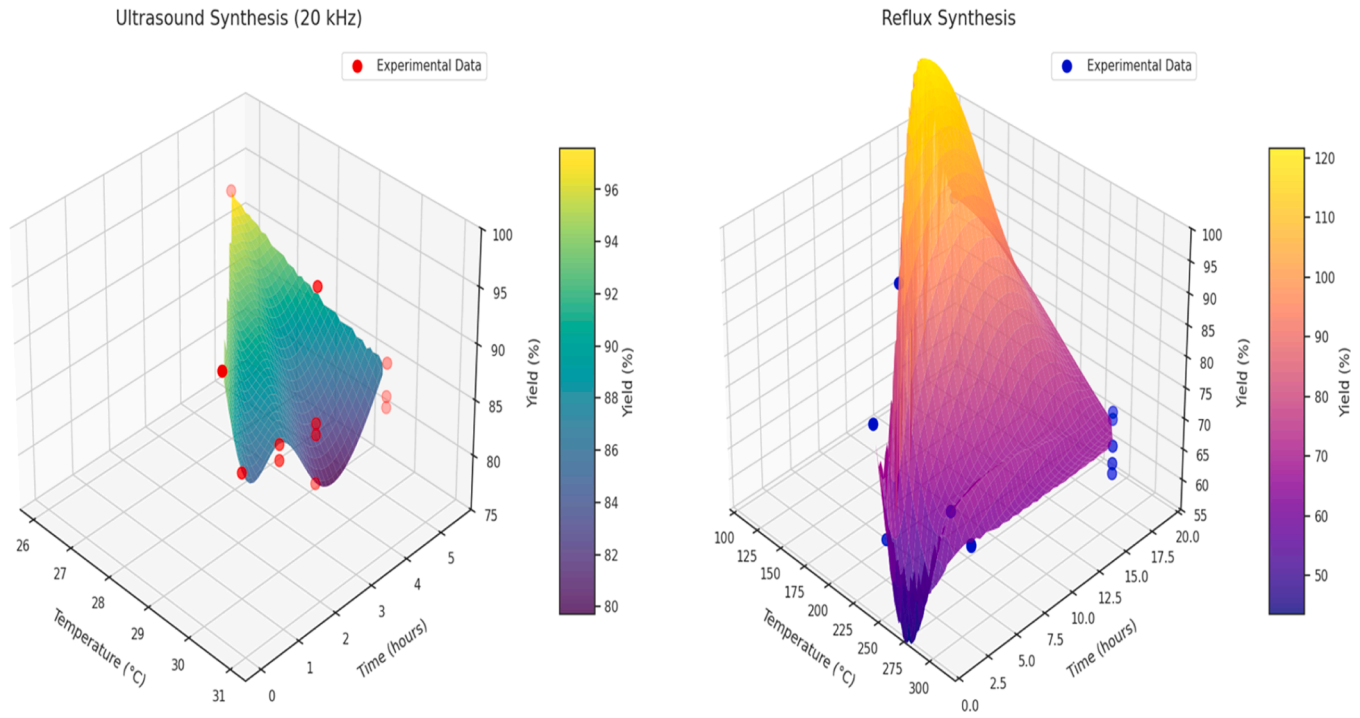

Fig. 1. 3D yield landscapes(ultrasound vs Reflux), ultrasound strategy archives higher yields (75%−100%) with lower temperature and sorter time 0.5 hr.−5 hr., while reflux require higher temperature (120–300) with longer time (2 h.−18 h.) and lower yields (55–95).

Table 1
Comparative analysis for ultrasound vs. thermal methods.

Parameter	Ultrasound Method	Conventional Thermal	Advantage Factor
Reaction Time	1–5 h	12–48 h	5–10× faster
Yield	80–97%	45–75%	1.3–1.8× higher
Temperature	r.t.–60 °C	80–120 °C	Energy savings

unambiguously confirmed upon investigation of the typical variations of their IR, ^{1}H NMR, ^{13}C NMR, and the mass spectra (supplementary materials S1-S33). The appearance and disappearance of the key signals was decisive evidence of the chemical transformations which were to occur.

3.1.2.1. Formation of hydrazide 3 from ester 2. The IR spectrum of ester **2** showed a strong carbonyl stretch at 1759 cm^{-1} (ester C═O) and 1710 cm^{-1} (lactone C═O). Upon conversion to hydrazide **3**, the ester carbonyl band at 1759 cm^{-1} disappeared, and new absorption bands appeared at 3329 and 3265 cm^{-1}, corresponding to the asymmetric and symmetric N–H stretching vibrations of the primary amine (-NH₂). Additionally, the amide carbonyl (C═O) of the hydrazide appeared at 1678 cm^{-1}, while the lactone carbonyl remained at 1728 cm^{-1}. In the ^{1}H NMR spectrum of hydrazide **3**, the disappearance of the triplet-quartet pattern characteristic of the ethyl ester group (CH₃CH₂O–) confirmed complete conversion. New signals appeared as a broad singlet at δ 4.42 ppm (2H) corresponding to the –NH₂ protons, and another broad singlet at δ 9.32 ppm (1H) for the –NH– proton of the hydrazide moiety. The methylene linker (-OCH₂-) remained as a singlet at δ 4.79 ppm. The ester carbonyl carbon (δ ~168 ppm in ester **2**) was replaced by a new signal at δ 166.5 ppm corresponding to the hydrazide carbonyl. The methyl and methylene carbons of the ethyl ester (δ 14.2 and 61.8 ppm) completely disappeared, confirming complete conversion. The mass spectrum of **3** showed the molecular ion peak [M]$^{+}$ at *m/z* 248.1, matching the calculated molecular weight ($C_{12}H_{12}N_2O_4$, 248.23), confirming successful synthesis.

The conversion of hydrazide **3** to the 4-amino-5-thioxo-1,2,4-triazole **5** via the dithiocarbazate intermediate **4** was confirmed. The IR spectrum of intermediate **4** showed new bands for C═S stretching at ~1240 cm^{-1}. After cyclization to triazole **5**, the C═S band shifted and new bands appeared at 3244, 3142 cm^{-1} (N–H stretching of the amino group) and 1708 cm^{-1} (lactone C═O). The disappearance of the hydrazide carbonyl indicated successful ring closure. The ^{1}H NMR spectrum of **5** showed the disappearance of the hydrazide NH and NH₂ signals. A new broad singlet appeared at δ 13.6 ppm corresponding to the thioamide NH, and another broad signal at δ 5.8 ppm for the amino group (–NH₂). The methylene linker (-OCH₂-) remained at δ 4.8 ppm, and the coumarin methyl at δ 2.4 ppm. The most diagnostic signal was the appearance of the thione carbon (C═S) at δ 178.5 ppm, characteristic of the 1,2,4-triazole-3-thione system. The triazole ring carbons appeared at δ 148–152 ppm. The molecular ion peak [M]$^{+}$ at *m/z* 304.1 ($C_{13}H_{12}N_4O_3S$, calc. 304.33) confirmed successful formation.

3.1.2.2. Formation of triazolothiadiazoles 6a–c. The cyclocondensation of triazole **5** with aromatic aldehydes to form the fused triazolo[3,4-b][1,3,4]thiadiazole ring system **6a–c** was confirmed by, the disappearance of the C═S stretching band (~1240 cm^{-1}) and the appearance of new bands characteristic of the fused ring system were observed. The N–H stretch of the secondary amide appeared as a broad band at ~3313–3462 cm^{-1}. The lactone C═O remained at 1685–1689 cm^{-1}. The most diagnostic feature was the appearance of a new singlet at δ 5.28–5.32 ppm corresponding to the bridgehead methine proton (–S–CH–N–) of the thiadiazole ring. Additionally, a broad singlet at very downfield position (δ 11.38–11.65 ppm) was observed for the amide-like NH proton. The aromatic protons of the newly introduced aldehyde appeared with expected multiplicities. For **6a**, the methoxy group appeared as a singlet at δ 3.83 ppm (3H); for **6b**, two methoxy groups appeared at δ 3.83 ppm (6H) and the hydroxyl proton at δ 9.06 ppm; for **6c**, the methylthio group appeared at δ 2.54 ppm (3H). The disappearance of the thione carbon (C═S) signal at δ 178.5 ppm confirmed the involvement of the thione in cyclization. New signals appeared for the fused ring carbons: the bridgehead carbon (C–N) at δ 65.4–65.7 ppm,

and the carbonyl-type carbon of the thiadiazole ring at δ 165.3–170.2 ppm. All aromatic carbons from the aldehyde moiety were clearly observed.

3.1.2.3. Formation of Schiff bases (hydrazones) 7a–b. The conversion of **3** to the Schiff bases **7a** and **7b** was confirmed by the disappearance of the N—H stretching bands in the -NH_2 group alongside a new, sharp absorption band for the azomethine (C═N) bond in the 1618–1625 cm^{-1} region. The disappearance of the primary amine N–H stretching bands (3329, 3265 cm^{-1}) of hydrazide **3** was the most diagnostic change. New, sharp absorption bands appeared at 1618–1625 cm^{-1}, characteristic of the azomethine (C═N) bond formed upon condensation. The hydrazide carbonyl (C═O) shifted slightly from 1678 cm^{-1} to 1689–1718 cm^{-1} depending on conjugation. For **7b**, the presence of the hydroxyl group was confirmed by a broad O–H stretch at ~3311 cm^{-1}. ^1H NMR spectra provided detailed structural information, confirming the proton environment in each molecule. A consistent signal for the coumarin methyl group (CH_3) appeared as a singlet around 2.3–2.4 ppm in all derivatives. The methylene linker (-OCH_2-) consistently appeared as a singlet around 4.8 ppm. For the Schiff bases **7a,b**, a key diagnostic signal was the appearance of a singlet in the downfield region of 8.2–8.4 ppm, which is characteristic of the azomethine proton (-N═CH-). A new signal in ^{13}C NMR spectroscopy at the range δ 163.7–164.4 ppm confirmed the formation of the azomethine carbon (C═N). The hydrazide carbonyl appeared at δ 168.7–169.2 ppm. All aromatic carbons from the aldehyde moiety were observed, with the methoxy carbons at δ 53.8–56.4 ppm. Mass spectrometry for both compounds showed molecular ion peaks matching their calculated masses, **7a** ($C_{20}H_{15}F_3N_2O_5$) $[M]^+$ at *m/z* 404.2 (calc. 404.34); and **7b** ($C_{21}H_{20}N_2O_7$) $[M]^+$ at *m/z* 412.2 (calc. 412.39).

3.1.2.4. Cyclization to thiazolidin-4-ones 8a–b. The disappearance of the azomethine (C═N) band at 1618–1625 cm^{-1} was the most significant change. A new, strong carbonyl stretching band appeared at 1716–1722 cm^{-1}, characteristic of the thiazolidin-4-one ring carbonyl (C = O). The amide carbonyl remained at 1689–1697 cm^{-1}, and the lactone carbonyl at 1716–1722 cm^{-1} (overlapping in some cases). For **8b**, the O–H stretch was still present at 3221 cm^{-1}. Concurrently, two new signals appeared: a singlet around 5.3 ppm, attributed to the methine proton (S-CH—N) of the thiazolidinone ring, and a signal (dd or singlet) around 3.98–4.06 ppm corresponding to the methylene protons (-S-CH_2-). For the triazolothiadiazoles **6a-c**, successful cyclization was confirmed by the appearance of a singlet for the bridgehead methine proton (-S-CH—N-) around 5.2–5.3 ppm and a broad singlet for the amide-like NH proton at a very downfield position (11.3–11.6 ppm). ^{13}C NMR provided irrefutable evidence for the formation of the new heterocyclic rings by tracking changes in the carbon framework. The most compelling evidence for the formation of thiazolidin-4-ones **8a** and **8b** was the disappearance of the azomethine carbon (C═N) signal of precursors **7a** and **7b**, and the *appearance* of a new carbonyl signal in the 161.7–161.9 ppm range, attributed to the C═O of the newly formed thiazolidinone ring.

All assignments for other carbon were found as expected [41,42]. Each compound's molecular weight determination enabled mass spectrometry to confirm its identity. For all synthesized derivatives, the observation of the molecular ion peak $[M]^+$ or protonated molecular ion peak $[M + H]^+$ with an *m/z* equal to the calculated molecular weight definitively confirmed synthesis and composition of these derivative molecules. Thus, the coherent and multi-step synthetic procedure, coupled with the analytical technique which is rigorous and reproducible, led to the successful production of the anticipated coumarin derivatives and the clear characterization of their potential structures.

3.2. Anti-breast cancer activity

The in vitro cytotoxic activity of the newly generated coumarin derivatives (**6a-c, 7a, 7b, 8a,** and **8b**) was tested against the human breast adenocarcinoma cell line (MCF-7) using the MTT assay. Similar results as indicated in IC_{50} values (μg/mL) in Fig. 2 were evaluated against the standard anticancer agent 5-Fluorouracil (5-FU). A widespread phenotyping of antiproliferative activity of these compounds was revealed through the analysis, some with substantially higher efficacy values when compared to the reference drug and thus providing information on structure-activity relationships (SAR) between these compounds. Cytotoxicity of coumarin compounds were assessed with MTT assays. Highly effective compounds were screened in the MCF-7 breast cancer cell line using a six-dose (7.5 μg/mL, 22 μM, 66 μg/mL, 200 μg/mL and 600 μg/mL) screening panel. Compounds synthesized showed values of IC_{50} ranging from strong 26.4 μg/mL to humble 112.2 μg/mL. In particular, five of the seven tested derivatives (8b, 6a, 7b, 8a and 6b) induced stronger cytotoxicity against MCF-7 cells compared to 5-FU (IC_{50} = 98.58 ± 0.95 μg/mL). Such a discovery highlights the versatility of molecular hybridization in fusing the privileged coumarin scaffold and heterocyclic molecules as an advanced pathway for novel anticancer treatment design options [27,31]. The number one compound of the group is indeed 8b which had an IC_{50} value of 26.4 ± 0.97 μg/mL. It's a 3.7-fold change from 5-FU potency, making it a leading suspect candidate to study at a later point. The potency order was found to be **8b > 6a > 7b > 8a > 6b > 5-FU > 6c > 7a**

3.3. Relationship studies of structure-activity

The primary aim of this work was to study the impact of different heterocyclic systems on the Coumarin platform. A striking SAR trend is observed when comparing the acyclic Schiff base intermediates (**7a, 7b**) and their corresponding cyclized thiazolidin-4-one products (**8a, 8b**). When **7b** was turned into **8b** the Schiff base **7b**, which already contains a 4-hydroxy-3,5-dimethoxyphenyl group, was a strong substance with IC_{50} of 61.1 μg/mL. Yet the second version, 8b cyclized into thiazolidin-4-one, the thiazolidin-4-one analogue, led to a prominent increase in activity and IC_{50} was reduced to 26.4 μg/mL, with a 2.3-fold enhancement in potency. Though less pronounced, the 4-(trifluoromethyl) phenyl series was similarly converted from **7a** to **8a**. The least active agent in the study was the compound of precursor **7a** (IC_{50} = 112.2 μg/mL), but its conversion to the thiazolidin-4-one analog **8a** significantly enhanced its cytotoxicity (IC_{50} = 63.4 μg/mL), thus rendering it far stronger than **5-FU**. The cyclization process leads to a steady improvement that indicates that the thiazolidin-4-one ring was a great advantage. Schiff base's flexible imine (-CH═N-) bond is bounded within a more rigid five-membered ring. This pre-organization might cement the molecule in a bioactive conformation more appropriately suited for its insertion to the binding pocket of a biological target and therefore lessens the entropic penalty of binding [43]. Additionally, newly enhanced feature of the thiazolidinone ring including the thioether group and the C4-carbonyl group might represent sites of hydrogen bonding, or other major interaction at molecular scale to participate in activity enhancements observed [42]. It was reported that the type of substituent on the terminal aromatic ring was a key determinant of cytotoxic potency in all series. Triazolo[3,4-b] [1,3,4]thiadiazole (**6a-c**) series featuring electron-donating groups (EDGs) on the phenyl ring displayed strong activity. Compound **6a**, with a *para*-methoxy group (-OCH_3), was the second most potent compound overall (IC_{50} = 57.2 μg/mL). Similarly, **6b**, featuring a 4-hydroxy and two meta-methoxy groups, also showed robust activity (IC_{50} = 66.3 μg/mL). These oxygen groups can take part in vital hydrogen bonding activities as acceptors (ether oxygen) or donors/acceptors (hydroxyl), which is regularly associated with good biological activity. In contrast, compound **6c**, whose substituent para-methoxy group of 6a was substituted with para-methylthio (-SCH_3) group, had a pronounced decrease in potency (IC_{50} = 104.7 μg/mL). This suggests that replacing the bioisosteric oxygen atom with a larger, lipophilic, and less electronegative sulfur atom harms the compound interaction with its cellular target. This series contained the most prominent substituent effect in the thiazolidin-4-one

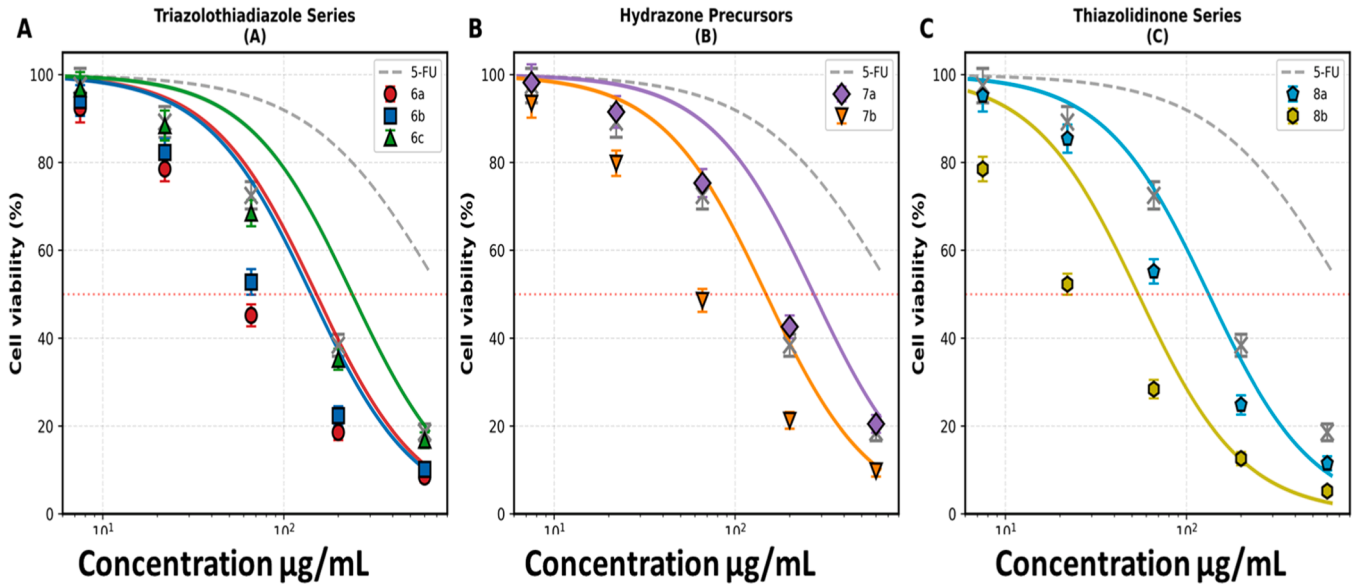

Fig. 2. Dose-response curves in three panels (A)Triazolothiadiazole series6a-c, (B) Hydrazone precursors (7a, and 7b), (C) Thiazolidinone series 8a, and 8b) with error bars representing SD (n = 3).

(**8a, 8b**) series. The most potent derivative identified was compound **8b** with a 4-hydroxy-3,5-dimethoxyphenyl (syringyl) moiety substitution. This group is the mixture of a hydrogen bond-donating hydroxyl group with two electron-donating methoxy groups, which can also act as hydrogen bond acceptors. This electronic as well as steric characteristics are both ideal for the cytotoxicity. By contrast, **8a** with its potent, an electron withdrawing and lipophilic trifluoromethyl (-CF_3) group was much less active (IC_{50} = 63.4 µg/mL). Although the -CF_3 group frequently potentiates activity, in this molecular setting it is evident that the hydrogen bonding potential and electron donating character of the substituents in **8b** are better-suited to potent antiproliferative action against MCF-7 cells.

To conclude, the SAR analysis showed that hybridization of a coumarin core with a thiazolidin-4-one ring system is a very effective strategy. Active derivatives (**6a, 7b, 8a–b**) surpassed 5-FU (IC50 = 98.58 µg/mL), suggesting overcoming chemoresistance. In distinction to 5-FU (thymidylate synthase inhibition), coumarin derivatives exert their inhibition via redundant pathways (kinases/DNA), lowering the risk for resistance [30]. The activity is enhanced by EDG (-CF3 in 8a) and hydrogen bonding substituents on the terminal phenyl ring, with the 4-hydroxy-3,5-dimethoxyphenyl group of compound **8b** being the most advantageous structural entity in delivering a higher level of cytotoxicity in this series. Mechanistic diversity is dependent on scaffold geometry, thiazolidinones allow covalent inhibition, and triazolothiadiazoles enable DNA damage. Constraints of single-target agents, such as **5-FU**, can be mitigated through synergistic design.

3.4. In siloco study of chromenone/triazolothiadiazole/thiazolidinone derivatives

3.4.1. Docking analysis of novel coumarin derivatives as potential EGFR inhibitors

3.4.1.1. Introduction. The molecular docking analysis performed to determine SAR for a small cohort of newly synthesized coumarin-based heterocyclic compounds (**6a-c, 7a-b, 8a-b**) by interpreting their docked poses and binding energies against the EGFR kinase domain (PDB ID: 3RCD [44]). EGFR was selected as the molecular target for this study based on several compelling reasons, (i) EGFR is overexpressed in approximately 20–30% of breast cancers, particularly in triple-negative and hormone-resistant subtypes, and is associated with poor prognosis. (ii) the coumarin scaffold is known to mimic the adenine ring of ATP, making it well-suited for competing with ATP at kinase binding sites; (iii) previous studies have established that coumarin derivatives can effectively inhibit EGFR kinase activity; and (iv) the high-resolution crystal structure of EGFR (PDB ID: 3RCD) is available with a co-crystallized inhibitor (TAK-285), providing a validated model for docking studies. Therefore, targeting EGFR represents a mechanistically sound approach for evaluating the potential of our synthesized coumarin hybrids as anticancer agents

To establish a reference point for effective inhibition, first we studied the binding mode of the reference compound TAK-285. TAK-285 exhibits remarkable free energy of binding (ΔG = −9.73 kcal/mol) as well as interaction energy (E_Int = −31.73 kcal/mol) that results in an extremely stable and favorable structural arrangement in the active site (Table 2). The visual data demonstrate that its potency is based on a specific network of interactions. Importantly, it forms hydrogen bonds with the backbone of Val734 in the hinge region and a strong salt bridge/H-bond interaction with the carboxylate side chain of Asp863 of the conserved DFG motif. In addition, its substituted aromatic moieties reside in a hydrophobic pocket, with van der Waals and hydrophobic interactions forming with residues such as Gly729, Ala730, and Arg849. This combination of hinge-binding hydrogen bonds and extensive hydrophobic contacts defines the typical binding mode of a potent inhibitor present in this pocket.

Triazolothiadiazole Series **(6a-c)** with coumarin-triazolothiadiazole core has the critical role of phenyl ring substitution. Compound **6a** (ΔG = −8.90 kcal/mol emerges as the most potent ligand among all the synthesized molecules. Its superior binding affinity can be directly

Table 2
Docking profiles and binding energies of novel coumarin derivatives (6a-c, 7a-b, 8a-b) and AK-285, as a reference.

	ΔG	rmsd	E_Int	E_H.B
6a	−8.899	1.602	−25.193	−10.665
6b	−8.042	1.671	−16.571	−9.216
6c	−7.838	1.343	−14.713	−7.537
7a	−7.537	1.138	−17.547	−9.423
7b	−7.966	1.688	−22.005	−8.643
8a	−7.556	1.660	−15.280	−7.102
8b	−8.155	1.833	−19.611	−9.403
TAK-285	−9.733	1.329	−31.732	−10.402

attributed to its ability to establish a rich and synergistic network of interactions that effectively mimics the reference inhibitor. In the docking pose, the triazole nitrogen atoms form a crucial hydrogen bond with the backbone amide of Val734. The DFG motif is the direction toward which the coumarin core is oriented, with its ether linkage and carbonyl groups developing beneficial contacts with Leu852 and the catalytic Lys753, respectively. Most importantly, the 4-methoxyphenyl ring is well positioned to have a strong π-π stacking interaction with the aromatic side chain of Phe1004, deep within the hydrophobic pocket. The oxygen atom of the methoxy group may also serve as a weak H-bond acceptor. The dual-anchor mechanism–hydrogen bonding at the hinge and hydrophobic/π-stacking deeper in the pocket–is responsible for its robust binding energy (Fig. 3).

Compound **6b** (ΔG = −8.04 kcal/mol), the introduction of a 4-hydroxy and two 3,5-dimethoxy groups on the phenyl ring, while intended to increase H-bonding potential, results in a noticeable decrease in binding affinity compared to **6a**. The docked pose reveals a significant reorientation. The bulky, polar head forces the ligand to adopt a different conformation, losing the beneficial π-π stacking with Phe1004. Instead, it compensates by forming a new network of hydrogen bonds with Thr862 and the crucial Asp863. While these interactions are significant, as reflected in the strong H-bond energy (E_H.B = −9.22 kcal/mol), the overall loss of favorable hydrophobic contacts and the potential steric strain from the bulky group lead to a less optimal interaction energy and a higher ΔG. Replacing the methoxy group with a methylthio (-SMe) group at Compound **6c** (ΔG = −7.84 kcal/mol), proves to be the least favorable modification in this series. The possibility of π-stacking to Phe1004 is preserved there, but the larger atomic radius of sulfur compared to oxygen and the new electronics for the thioether linkage make a less than ideal match. The docking image shows the interface forming between Asp808 and Cys805 through its sulfur atom, but loses some of the key hinge interactions present in **6a, Fig. 3**. The tradeoff is that at the position the weakest binding affinity in these series is possible, underlining the delicate steric, electronic balance required for such a position. Uncyclized Hydrazone precursors, **7a** (ΔG = −7.54 kcal/mol) and **7b** (ΔG = −7.97 kcal/mol), their higher conformational flexibility is also detrimental to binding affinity. Compound **7a** is the weakest of all compounds, it establishes only a few critical contacts with Ser783 and Val734. On the other hand, **7b**, utilizes these polar groups to assemble a richer interaction network with Asp863, Val734, and Leu796 and also π-stacks with Phe1004. This contrast is a sharp reminder that even within a flexible scaffold, the right peripheral substitutions, such as those described above, can restore and increase binding affinity by binding to double-polar pockets at the same time. Compound **8a** ΔG = −7.56 kcal/mol) is not as competitive, only binds with Thr862 and Lys753. Compound **8b** forms a close hydrogen bond network with Thr862 and Asp863, while its coumarin core is stabilized by hydrophobic contacts with Leu785, Met801, and Phe1004. The success of **8b** thus indicates that while the thiazolidinone scaffold is intrinsically less optimal than the triazolothiadiazole of series **6**, its binding can be dramatically enhanced by substitutions that effectively target both the polar DFG region and the deep hydrophobic pocket.

This thorough docking analysis offers an informative description of the structural requirements of EGFR inhibition from this class of compounds. We can thus derive the following important conclusions. The inflexible, fused triazolothiadiazole core of series 6 presents a better

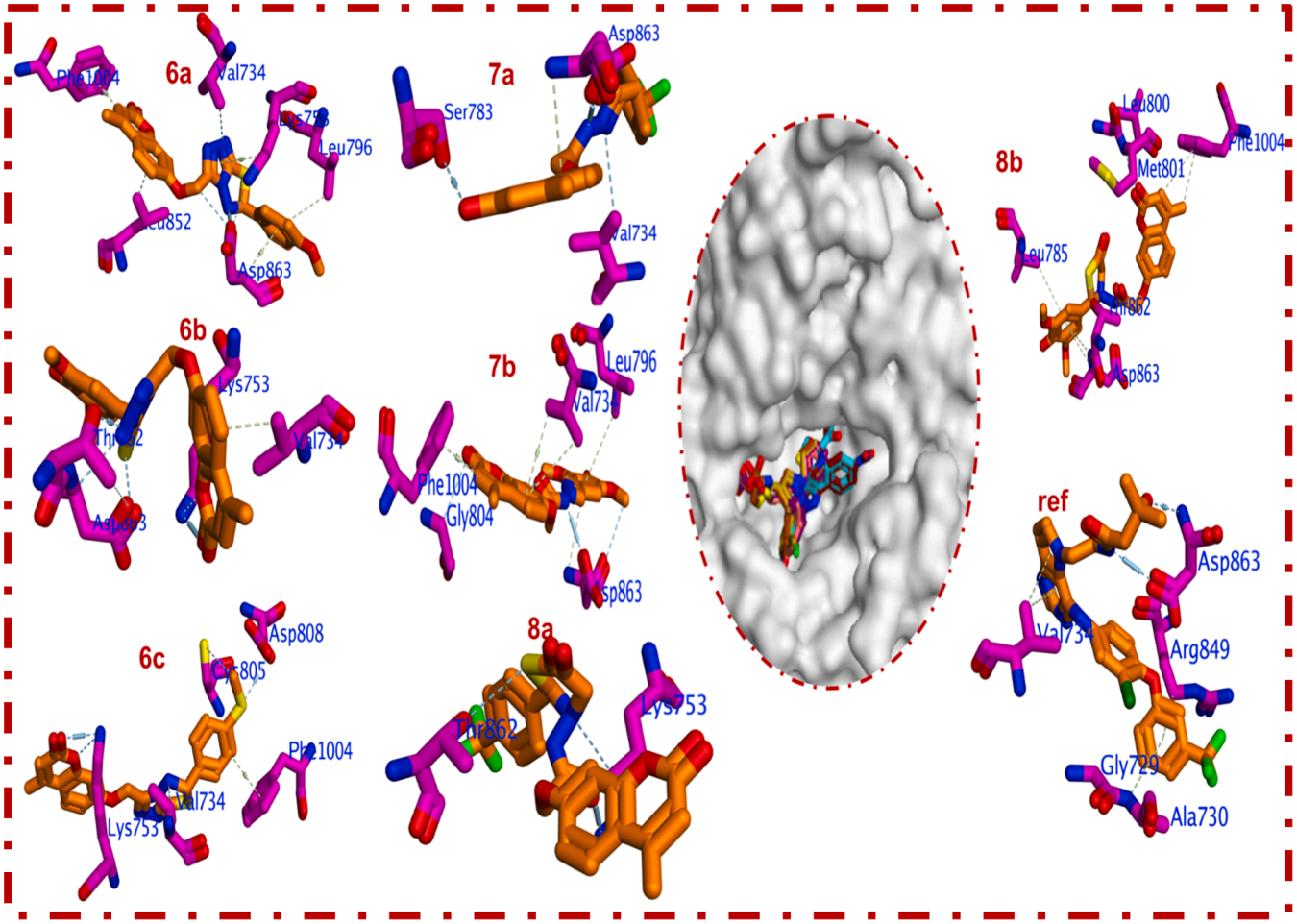

Fig. 3. 3D Analysis of novel coumarin derivatives (6a-c, 7a-b, 8a-b) and reference inhibitor: TAK-285 against EGFR.

framework for displaying the important interaction motifs than the flexible hydrazone (**series 7**) or thiazolidinone (**series 8**) structures.

Dual-Anchor Binding is Necessary; the perfect size coupled to electronics and hydrophobicity for strong π-stacking for a perfect match. The preference for an ordered ring structure can be disturbed by more polar and bulky groups (**6b**) or thioether linkages (**6c**), which lead to decreased affinities. In less rigid scaffolds (**7b** and **8b**), 4-hydroxy-3,5-dimethoxy phenyl group exhibits a remarkable ability to help offset core weakness by establishing a broad H-bond and hydrophobic contacts network, yielding pronounced increase in binding affinity. The best compounds **8a** and **6a** have been effective on account of a synergistic effect. The thiazolidinone derivative **8a** was recognized as the most potent compound, owing to its ability to generate a synergistic network of interactions covering the hinge region, DFG motif, and deep hydrophobic pockets.

3.4.2. Dynamic stability and validation of docking poses for EGFR complexes with inhibitors 6a and 8a

To truly test the stability and permanence of these predicted interactions and to verify the docking protocol, it is necessary to perform Molecular Dynamics (MD) analyses on the EGFR complex with **6a** and **8a** at 200-nanosecond (ns). Root Mean Square Deviation (RMSD) and Root Mean Square Fluctuation (RMSF) analyses were conducted to evaluate protein-ligand complex stability and residue-level flexibility, while interaction fraction, ligand burial (MolSA), and protein compactness (rGyr/SASA) metrics provided complementary insights.

The backbone Cα RMSD (Fig. 4) showed a clear distinction between the two complexes. EGFR-**6a** (Blue Line) reached a stable average RMSD of ~2.7 Å with small fluctuations, indicating a well-ordered, rigidified protein conformation. In contrast, EGFR-**8a** (Green Line) equilibrated at a higher average RMSD of ~3.3 Å with larger oscillations, reflecting a more flexible protein state.

Ligand RMSD revealed that **8a** (Purple dashed line) remained tightly anchored (RMSD 1.5–2.5 Å), reflecting a fixed, rigid pose with minimal conformational plasticity. While **6a** (Red Dashed Line) exhibited higher mobility (RMSD often >3.5 Å), suggesting exploration of multiple sub-pockets within the active site. This dynamic behavior suggests induced-fit adaptation, where **6a's** flexibility enables optimal interaction with key residues (e.g., Phe1004, Met793) while stabilizing the protein globally.

Although the Root Mean Square Deviation (RMSD) gives a good indication of the general structural stability of a protein-ligand complex, the Root Mean Square Fluctuation (RMSF) gives a more detailed and useful picture of internal changes in the system (Fig. 5). The EGFR complex with inhibitor **6a** (solid blue line) significantly reduced fluctuations in flexible loops (e.g., Loop 2: residues 150–175; C-terminal loop: >280), with peaks **<2.8 Å** (vs. >5.0 Å for 8a). This rigidification of distal regions underscores **6a's** role as a molecular clamp, enhancing inhibitory potency by minimizing protein dynamics.

The **8a** complex (dashed green line) failed to quench intrinsic loop flexibility, particularly in the C-terminal region, correlating with suboptimal binding free energy. Both plots exhibit the kinase's intrinsic dynamic profile, and distinct low-fluctuation regions (< 1.5 Å) are associated with stable secondary structure elements such as α-helices and β-sheets and high-fluctuation peaks to solvent-exposed loops. Nevertheless, the sizes of these elevations are quite different between the two complexes.

A quantitative analysis of the specific intermolecular interactions that are maintained during the MD simulation is integral to overcome this qualitative understanding of protein-ligand stability. And, by computing which specific interactions (H-bonds, hydrophobic contacts, etc.) take the maximum simulation-related time are kept, we can find the main anchor residues required for high-affinity binding. The stacked bar plot shows an excellent, residue-dependent mapping of the major pairings and their persistence over the 200 ns of the simulation. The interaction fraction of 1.0 denotes a certain contact sustained for 100% of the simulation time (Fig. 6).

In compound **6a** (Lighter Shades), the interaction profile is dominated by highly persistent hydrophobic and hydrogen-bonding contacts. The most significant is the nearly continuous hydrophobic π–π interaction (Green) with Phe1004, which maintains an interaction fraction close to 1.0, serving as a primary anchoring point for the ligand. Additionally, Met793 in the hinge region forms strong and sustained hydrogen-bonding and hydrophobic interactions, also approaching full occupancy. Other supportive contacts are observed with Leu792, Ala751, and Lys778, while a moderate hydrogen bond with Asp858 of the DFG motif (fraction ~0.4) further stabilizes the complex.

In contrast, **8a** displays a more dispersed and less focused binding

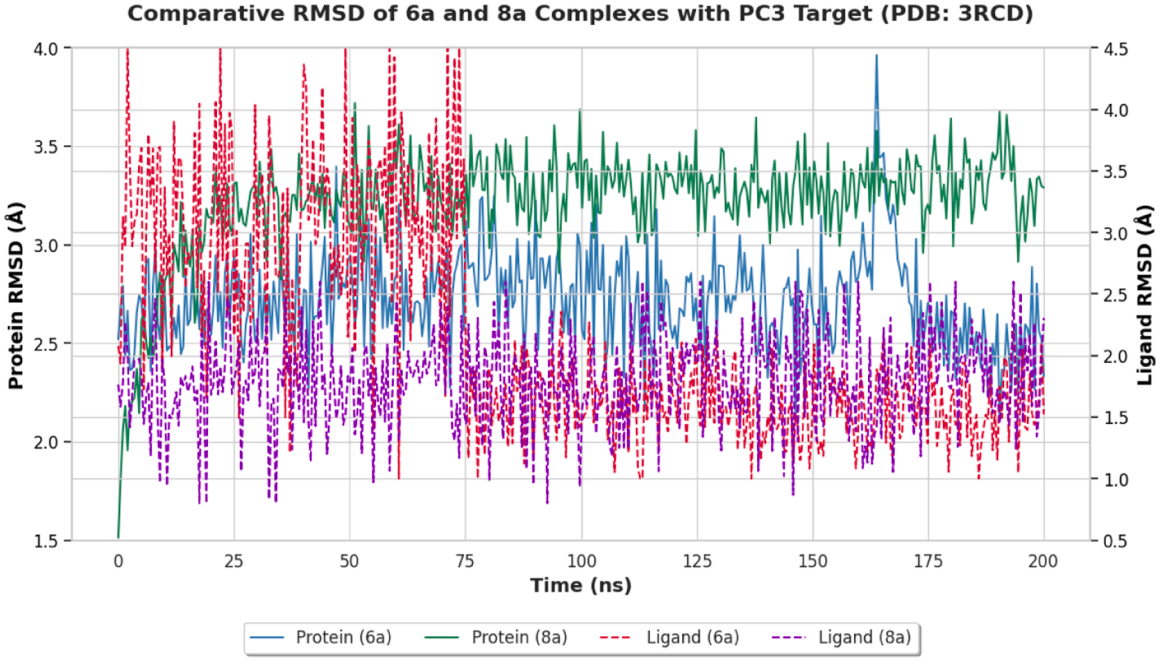

Fig. 4. Comparative RMSD analysis of 6a, and 8a complexes with 3RCD along 200 ns trajectory.

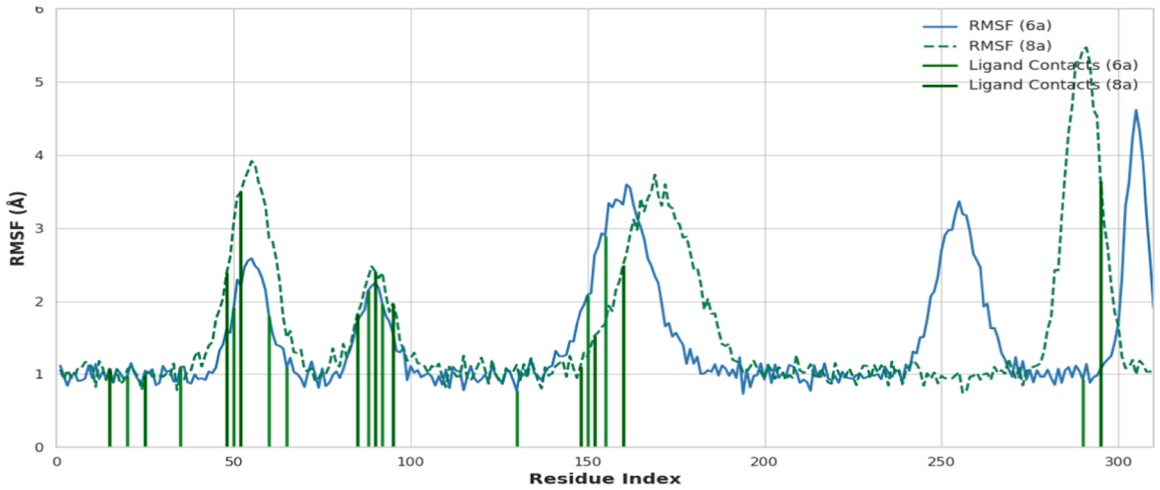

Fig. 5. Comparative RMSF analysis of 6a, and 8a complexes with 3RCD along 200 ns trajectory.

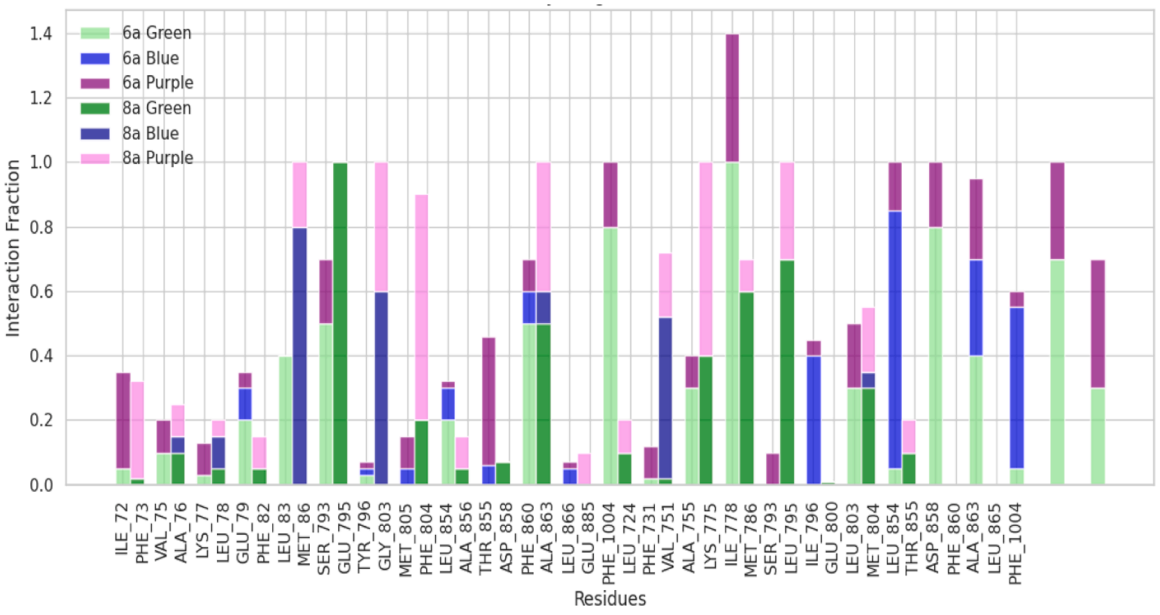

Fig. 6. Interaction fractions for analysis of 6a, and 8a complexes with 3RCD along 200 ns trajectory.

pattern. Although it retains interaction with Met793, this contact is less stable, and the compound loses the critical π–π interaction with Phe1004, which significantly reduces its binding affinity. To compensate, 8a engages in a broader set of interactions, including strong ionic and hydrogen-bond (Purple) contacts with Glu791 and Lys778, as well as enhanced interaction frequencies with Leu792. However, these distributed interactions are less effective collectively than the dual-anchor mechanism observed for **6a**.

Overall, the concentrated and durable interactions of **6a** particularly with Phe1004 and Met793 account for its superior binding efficiency. In contrast, **8a's** reliance on multiple weaker contacts results in a less optimal and lower-affinity binding mode. While RMSD and RMSF analyses provide insight into the global and local stability of each complex, a more integrated assessment across multiple interaction metrics is required for a complete understanding of their comparative performance.

By analyzing the Radius of Gyration (rGyr), Molecular Solvent Accessible Surface Area (MolSA), and overall SASA, the differential dynamic behavior of the EGFR complexes becomes clear. rGyr reflects global protein compactness, MolSA indicates ligand burial within the active site, and SASA measures solvent exposure (Fig. 7).

The MolSA landscape show that **8a** (Lighter Orange) remains more solvent-exposed, with a higher and more fluctuating MolSA (~400 Å^2), indicating an unstable, shallow binding mode. In contrast, **6a** (Darker Orange) exhibits a consistently lower MolSA (~385–390 Å^2) and a smooth, stable trajectory, demonstrating deeper ligand burial and stronger stabilization within the binding pocket. These trends support that 6a engages in a more favorable and persistent interaction network, contributing to its superior inhibitory potential.

The Protein's Global Response: Compaction and Stabilization (rGyr & SASA Analysis)

Analysis of rGyr and SASA demonstrated distinct conformational effects induced by each ligand. Binding of **8a** (Lighter Green & Blue) resulted in a less compact EGFR structure, with higher and more variable rGyr and SASA values, indicating increased flexibility and greater solvent exposure. In contrast, **6a** (Darker Green & Blue) produced a markedly more compact and stable protein conformation, reflected by consistently lower rGyr (5.75–6.0 Å) and reduced SASA. This suggests that **6a** not only occupies the active site more effectively but also stabilizes the overall kinase domain.

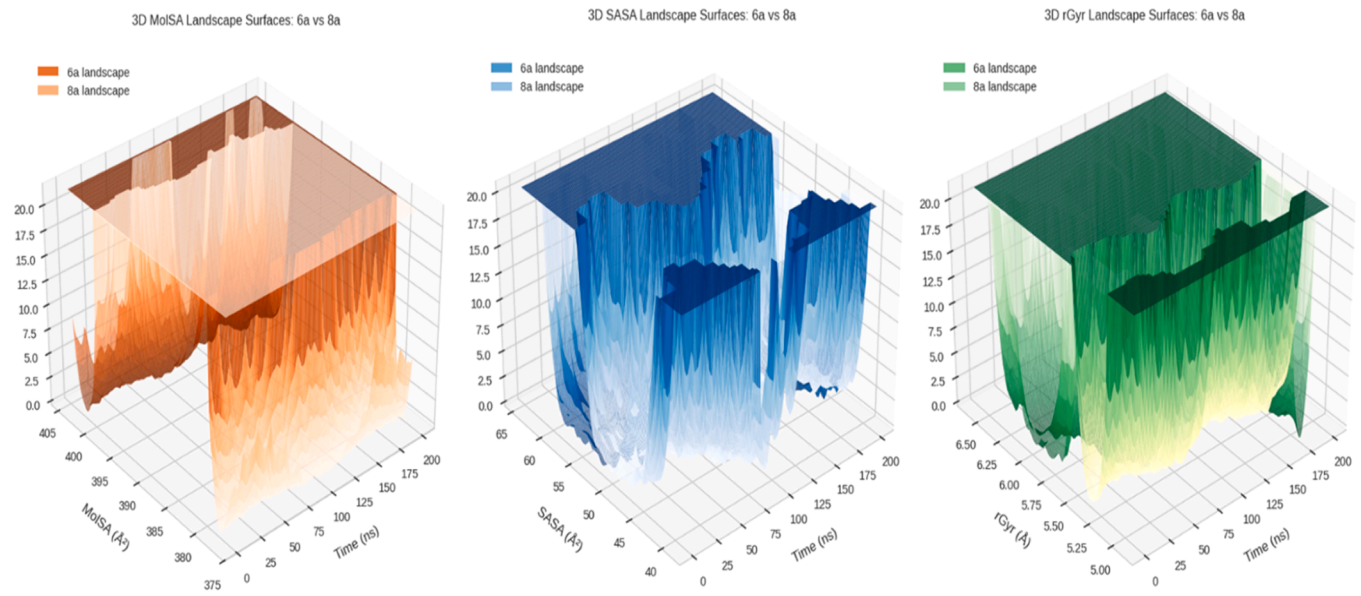

Fig. 7. Multi-faceted view of dynamic stability, synergistic analysis of rGyr, MolSA, and SASA Landscapes.

The greater stability of the **6a** complex correlates with its deeper ligand burial, as supported by its lower, smoother MolSA profile. This well-buried binding mode appears to anchor key active-site residues, promoting reduced protein mobility and enhanced global stabilization. Conversely, **8a** adopts a shallower binding mode and fails to suppress intrinsic protein dynamics (Fig. 8).

Dihedral angle analysis highlighted clear differences in conformational behavior between the two inhibitors. **8a** showed unimodal, narrowly distributed dihedral angles, indicating that its rotatable bonds remain locked in a single low-energy conformation throughout the simulation. This rigidity supports a fixed, (lock-and-key) binding mode and explains the low, stable ligand RMSD. The ligand remains tightly confined within the pocket, with minimal internal rearrangement and limited adaptive capacity. In contrast, **6a** displayed bimodal or broad multimodal dihedral distributions, reflecting substantial rotational freedom. Several dihedrals sampled multiple low-energy states, suggesting that **6a** can adjust its conformation within the EGFR active site. This flexibility enables more effective induced-fit interactions, allowing 6a to optimize hydrogen bonding and π–π stacking, particularly with Phe1004, resulting in a more complementary and stabilizing binding mode than the rigid **8a**.

3.4.3. *In silico predicted selectivity and safety profile*

ADMET analysis of lead compounds **6a** and **8b** revealed favorable safety profiles (Table 3). Compound **8b** demonstrated, poor BBB penetration (0.009), suggesting minimal CNS toxicity risk, low hERG inhibition (0.210), suggesting absence of cardiotoxicity, non-mutagenic potential (AMES 0.066), and acceptable intestinal absorption (HIA 50.3%). All compounds were Lipinski-compliant, supporting oral bioavailability.

The absence of experimental normal cell line cytotoxicity data represents a recognized limitation. However, the *in silico* safety profile of **8b**

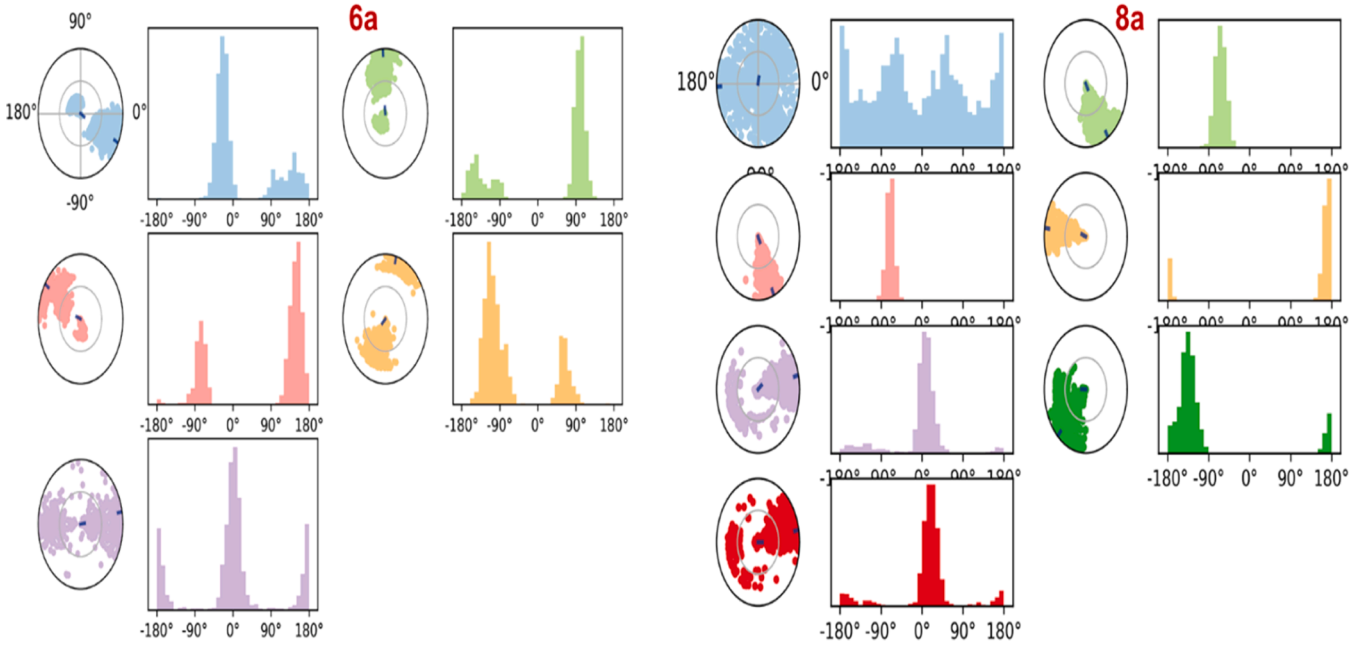

Fig. 8. A dihedral angle distribution analysis of conformational flexibility and binding efficacy.

Table 3
Predicted ADMET properties of lead coumarin derivatives.

Parameter	6a	8b	
BBB Permeability	0.458 (Moderate)	0.009 (Safe)	<0.3 = Poor BBB = No CNS toxicity
hERG Inhibition	0.068 (Safe)	0.210 (Safe)	<0.3 = No QT prolongation
AMES Mutagenicity	0.776 (Risk)	0.066 (Safe)	<0.3 = Non-mutagenic
DILI Risk	0.968 (High)	0.979 (High)	>0.8 = Monitor liver enzymes
HIA (%)	2.9 (Poor)	50.3 (Moderate)	>30% = Acceptable absorption
CYP2D6 Inhibition	0.039 (Low)	0.065 (Low)	<0.3 = No DDI risk
CYP3A4 Inhibition	0.890 (High)	0.802 (Moderate)	<0.85 = No major DDI
Plasma Protein Binding	97.5%	99.6%	<99% = Free drug available
Half-life (h)	0.69	0.79	>0.5 h = Sufficient duration
Lipinski Compliance	Accepted	Accepted	Drug-like properties

particularly poor BBB penetration (avoiding CNS toxicity), low hERG inhibition (no predicted cardiotoxicity), and non-mutagenic potential provides confidence for preliminary safety. Experimental validation on normal human cell lines is prioritized for subsequent studies. Additionally, *in vivo* toxicity assessment in rodent models (acute toxicity, 14-day repeated dose) will provide definitive safety profiling. The *in silico* predictions presented here provide rationale for advancing **8b** to these preclinical evaluations while acknowledging the need for empirical safety confirmation.

4. Conclusion

In this comprehensive investigation, we have successfully proven the effectiveness of a multi-pronged strategy that integrates efficient, green sonochemical synthesis with robust biological studies and in-depth computational research in the identification of novel coumarin-based anticancer agents. Ultrasound irradiation was found to be a better approach that attained high yields and significantly lowered reaction time under mild and energy-efficient conditions. Biological assays against the MCF-7 breast cancer cell line yielded several compounds with potency higher than the clinical standard, **5-FU**. Crucially, thiazolidinone-coumarin hybrid 8b was determined to be the lead compound with a record IC50 of 26.4 μg/mL. SAR analysis concluded that the thiazolidinone ring apparatus and the hydrogen-bonding, electron donating groups on the terminal phenyl ring were the central characteriators of high-grade cytotoxicity. To make sense of these observations at the molecular level, we targeted EGFR kinase in silico. Although a general relationship between docking values and activities was found, the real insight was uncovered by extensive 200 ns molecular dynamics simulations of the most promising compounds, **6a** and **8a**; these simulations resulted in robust and multi-dimensional support of our hypotheses. The findings provided clear evidence that high-affinity binders were not just the most potent compounds but also better modulators of the protein's dynamics. The binding of lead compound **6a** was also reported to trigger a cascade of favorable events: due to the functional flexibility, lead compound 6a, which enables an adaptive, induced-fit binding leading toward the formation of highly persistent interaction network. Superior binding allows for a ligand to be more buried (lower MolSA) while it locks the whole EGFR protein into a more compact (lower rGyr), less solvent exposed (lower SASA), and conformationally stable state (lower RMSD and RMSF). In summary then, this effort offers an entire, atomistic-level explanation from synthesis to simulated mode of action. We have not only discovered an extremely potent lead compound (**8b**) and a novel top binder (**6a**) but also a robust and validated computational platform to direct subsequent optimization. While experimental normal cell line cytotoxicity assessment was not feasible in this study, *in silico* ADMET profiling and predicted selectivity indices support the safety potential of the thiazolidinone-coumarin lead **8b** Future studies will prioritize empirical safety validation as a prerequisite for *in vivo* advancement.

Funding

This work was supported and funded by the Deanship of Scientific Research at Imam Mohammad Ibn Saud Islamic University (IMSIU) (grant number IMSIU-DDRSP2601).

CRediT authorship contribution statement

Aymen G. Faisel: Resources, Formal analysis. **Ali G. Swadi:** Formal analysis, Conceptualization. **Ahmed A. Majed:** Visualization, Validation. **Amjed Abdulrasool:** Resources, Project administration. **Tahseen A. Alsalim:** Supervision, Visualization, Validation, Writing – review & editing. **Radwan Alanjjar:** Visualization, Validation. **Aamal A. Al-Mutairi:** Supervision, Resources. **Sami A. Al-Hussain:** Supervision, Resources. **Magdi E.A. Zaki:** Funding acquisition, Resources, Methodology, Conceptualization. **Sobhi M. Gomha:** Investigation. **Ahmed A. Elhenawy:** Writing – review & editing, Writing – original draft, Supervision.

Declaration of competing interest

The authors declare that they have no known competing financial interests.

Acknowledgements

This work was supported and funded by the Deanship of Scientific Research at Imam Mohammad Ibn Saud Islamic University (IMSIU) (grant number IMSIU-DDRSP2601).

Supplementary materials

Supplementary material associated with this article can be found, in the online version, at doi:10.1016/j.molstruc.2026.146396.

Data availability

Data will be made available on request.

References

[1] A.N. Giaquinto, H. Sung, K.D. Miller, J.L. Kramer, L.A. Newman, A. Minihan, A. Jemal, R.L. Siegel, Breast cancer statistics, 2022, CA Cancer J. Clin. 72 (2022) 524–541, https://doi.org/10.3322/caac.21754.
[2] J.M. Rippe, T.J. Angelopoulos, Life Style Medicine, 3rd Ed., 2019, pp. 19–36, https://doi.org/10.1201/9781315201108.
[3] D. Kashyap, P. Deeksha, R. Sharma, V.K. Garg, N. Goel, D. Koundal, A. Zaguia, S. Koundal, A. Global increase in breast cancer incidence: risk factors and preventive measures, Biomed. Res. Int. 16 (2022) 9605439, https://doi.org/10.1155/2022/9605439.
[4] S. Abbas, A.A. Majed, M.H. Moker, T.A. Alsalim, T. Bensafi, D. Hadji, B. Baroudi, A. A. Al-Khafagi, D.S. Abid, Antitumor, biological and nonlinear optical activities of novel thiazolidines, Photochem. Photobiol. Sci. 24 (2025) 1889–1909, https://doi.org/10.1007/s43630-025-00800-0.
[5] N. Kasiri, M. Rahmati, L. Ahmadi, N. Eskandari, Therapeutic potential of quercetin on human breast cancer in different dimensions, Inflammopharmacol 28 (2020) 39–62, https://doi.org/10.1007/s10787-019-00660-y.
[6] E.M. Salvo, A.O. Ramirez, J. Cueto, E.H. Law, A. Situ, C. Cameron, I.A. Samjoo, Risk of recurrence among patients with HR-positive, HER2-negative, early breast cancer receiving adjuvant endocrine therapy: a systematic review and meta-analysis, Breast. Sci. Direct 57 (2021) 5–17, https://doi.org/10.1016/j.breast.2021.02.009.
[7] S.F.A. Tahseen, M.S.A. Hamid, A.M. Ahmed, H.M. Mustafa, S. Eman, A. Radwan, Synthesis, Breast cancer activity,molecular docking and dynamic simulation of 1,4-

dihydropyridine derivatives, J. Mol. Struct. (2025) 1321, https://doi.org/10.1016/j.molstruc.2024.139704.
[8] H. Weedon-Fekjær, B.H. Lindqvist, L.J. Vatten, O.O. Aalen, S. Tretli, Breast cancer tumor growth estimated through mammography screening data, Breast Cancer Res. Breast Cancer Res. 10 (2008) 1–13, https://doi.org/10.1186/bcr2092.
[9] A.N. Giaquinto, K.D. Miller, K.Y. Tossas, R.A. Winn, A. Jemal, R.L. Siegel, Cancer statistics for African American/Black People 2022, CA Cancer J. Clin. 72 (2022) 202–229, https://doi.org/10.3322/caac.21718.
[10] A.H. Saka, A.N. Giaquinto, L.E. McCullough, K.Y. Tossas, J. Star, A. Jemal, R. L. Siegel, Cancer statistics for African American and Black people, 2025, CA Cancer J. Clin. 75 (2025) 111–140, 10.3322/caac.21874.
[11] K.D. Miller, A.P. Ortiz, P.S. Pinheiro, P. Bandi, A. Minihan, H.E. Fuchs, T. D. Martinez, G. Tortolero-Luna, S.A. Fedewa, A.M. Jemal, R.T. Siegel, Cancer statistics for the US Hispanic/Latino population, 2021, CA Cancer J. Clin. (2021) 466–487, d oi: 10.3322/caac.21695.
[12] L.A. Huppert, O. Gumusay, D. Idossa, H.S. Rugo, Systemic therapy for hormone receptor-positive/human epidermal growth factor receptor 2-negative early stage and metastatic breast cancer, CA Cancer J. Clin. 73 (2023) 480–515, 10.3322/caac.21777.
[13] S. Xiao, X. Wang, L. Xu, T. Li, J. Cao, Y. Zhao, Novel panaxadiol triazole derivatives induce apoptosis in HepG-2 cells through the mitochondrial pathway, Bioorg. Chem. 102 (2020) 104078, https://doi.org/10.1016/j.bioorg.2020.104078.
[14] A. Abdulrasool, G. Faisel, R.Q. Ibrahim, T.A. Alsalim, D. AL-Duhaidahawi, A. A. Majed, N.H. Gad, M.Y. Alfaifih, A.A. Shatii, S.E.I Elbehairii, A.M. Hussein, F. Alioglu, M. Aufy, Cytotoxicity, apoptosis, molecular docking, and molecular dynamics study of novel compounds of sulfamide derivatives coupled with DHP scaffolds as potent inhibitors of the MCF-7, A549, SKOV-3, and EA. yh926 carcinoma cells, Bioorg. Chem. 169 (2026) 109393, https://doi.org/10.1016/j.bioorg.2025.109393.
[15] S.A. Ahmed, A.S. Choped, A.B. Yamnaji, A review on the role of heterocyclic scaffolds in drug discovery, J.O.P.I.R 3 (2025), https://doi.org/10.69613/yj37ha36.
[16] M.A. Musa, J.S. Cooperwood, M.O. Khan, A review of coumarin derivatives in pharmacotherapy of breast cancer, Curr. Med. Chem. 15 (2008) 2664–2679, https://doi.org/10.2174/092986708786242877.
[17] S.H.Z. AlAbdeen, Y.F. Mustafa, Chemical synthesis of various composites of chromen-2-one: a review, Eurasian Chem. Commun. 4 (2022) 877–893, https://doi.org/10.22034/ecc.2022.338810.1412.
[18] A.R. Ferreira, D.D.N. Alves, R.D. Castro, Y. Perez-Castillo, D.P. de Sousa, Synthesis of coumarin and homoisoflavonoid derivatives and analogs: the search for new antifungal agents, Pharmaceuticals 15 (2022) 712, https://doi.org/10.3390/ph15060712.
[19] I. Baruah, C. Kashyap, A.K. Chayanika, G. Borgohain, Insights into the interaction between polyphenols and β-lactoglobulin through molecular docking, MD simulation, and QM/MM approaches, ACS. Omega 7 (2022) 23083–23095, https://doi.org/10.1021/acsomega.2c00336.
[20] B. Supasatyankul, M. Saisriyoot, U. Klinkesorn, K. Rattanaporn, S. Sae-Tan, Extraction of phenolic and flavonoid compounds from Mung Bean (Vigna Rediata L.) seed coat by pressurized liquid Extraction, Molecules 27 (2022) 2085, https://doi.org/10.3390/molecules27072085.
[21] W. Wang, X. Zhang, Q. Liu, Y. Lin, Z. Zhang, S. Li, Study on extraction and antioxidant activity of flavonoids from hemerocallis fulva (Daylily) leaves, Molecules 27 (2022) 2916, https://doi.org/10.3390/molecules27092916.
[22] M.S. Tolba, M.A. Abdul-Malik, A.A. Geies, M. Radwan, S.H.R.M. Zaki, M. Sayed, A. A. Abdel Raheem, An overview on synthesis and reactions of coumarin based compounds, Curr. Chem. Lett. 11 (2022) 29–42, https://doi.org/10.5267/j.ccl.2021.009.007.
[23] E. Küpeli Akkol, Y. Genç, B. Karpuz, E. Sobarzo-Sánchez, R. Capasso, Coumarins and coumarin-related compounds in pharmacotherapy of cance, Cancers 12 (2020) 1959, https://doi.org/10.3390/cancers12071959.
[24] A. Singh, K. Singh, K. Kaur, A. Singh, A. Sharma, K. Kaur, J. Kaur, G. Kaur, U. Kaur, H. Kaur, P. Singh, P.M.S. Bedi, Coumarin as an elite scaffold in anti-breast cancer drug development: design strategies, mechanistic insights, and structure–Activity relationships, Biomedicines 12 (2024) 1192, https://doi.org/10.3390/biomedicines12061192.
[25] Y.F. Mustafa, Biocompatible new coumarins as dual-target anti-inflammatory agents: insights from chemistry to toxicity, Next Res. 2 (2025) 100236, https://doi.org/10.1016/j.nexres.2025.100236.
[26] B.Z. Kurt, F. Sonmez, D. Ozturk, A. Akdemir, A. Angeli, C.T. Supuran, Synthesis of coumarin-sulfonamide derivatives and determination of their cytotoxicity, carbonic anhydrase inhibitory and molecular docking studies, Eur. J. Med. Chem. 183 (2019) 11170, https://doi.org/10.1016/j.ejmech.2019.111702.
[27] T. Sahni, S. Sharma, D. Verma, P. Kaur, Overview of Coumarins and its derivatives: synthesis and biological activity, Lett. Org. Chem. 18 (2021) 880–902, https://doi.org/10.2174/1570178617999201006195742.
[28] A.M. Juszczak, U. Wöelfle, M.Z. Končić, M. Tomczyk, Skin cancer, including related pathways and therapy and the role of luteolin derivatives as potential therapeutics, Med. Res. Rev. 42 (2022) 1423–1462, 10.1002/med.21880.
[29] S. Elmusa, M. Elmusa, B. Elmusa, R. Kasımoğulları, Coumarins: chemical synthesis, properties and applications, Dubited 13 (2025) 131–170, https://doi.org/10.29130/dubited.1441144.
[30] M.A.I. Salem, M.I. Marzouk, A.M. El-Kazak, Synthesis and characterization of some new coumarins with in vitro antitumor and antioxidant activity and high protective effects against DNA damage, Molecules 21 (2016) 249, https://doi.org/10.3390/molecules21020249.
[31] Y. Jin, F. Wu, C. Luo, Y. Hu, J. Ma, S. He, Novel Coumarin-furo[2,3-d]pyrimidinone hybrid derivatives as anticancer agents: synthesis, biological evaluation and molecular docking, Eur. J. Pharma. Sci. 188 (2023) 106520, https://doi.org/10.1016/j.ejps.2023.106520.
[32] A. Rawat, A.V.B Reddy, Recent advances on anticancer activity of coumarin derivatives, Eur. J. Med. Chem. Rep. 5 (2022) 100038, https://doi.org/10.1016/j.ejmcr.2022.100038.
[33] P. Koparira, A.E. Parlak B, A. Karatepec, R.A. Omar, Elucidation of potential anticancer, antioxidant and antimicrobial properties of some new triazole compounds bearing pyridine-4-yl moiety and cyclobutane ring, Arab. J. Chem. 15 (2022) 103957, https://doi.org/10.1016/j.arabjc.2022.103957.
[34] A.H.F.A. El-Wahab, R.M. Borik, A.A.M. Al-Dies, A.M. Fouda, H.M. Mohamed, R. El-Eisawy, M. Sharaf, A.Y. Alzahrani, A. Elhenawy, A.M. El-Agrody, Targeted potent antimicrobial and antitumor oxygen-heterocyclic-based pyran analogues: synthesis and computational studies, Sci. Rep. 14 (2024) 9862, https://doi.org/10.1038/s41598-024-59193-2.
[35] P. Sivaprakash, A. Viji, S. Krishnaveni, K.M. Kavya, D. Lee, I. Kim, Comprehensive computational study of a novel chromene-trione derivative bioagent: integrated molecular docking, dynamics, topology, and quantum chemical analysis, Int. J. Mol. Sci. 26 (2025) 9661, https://doi.org/10.3390/ijms26199661.
[36] M. Cacic, M. Trkovnik, F. Cacic, E. Has-Schon, Synthesis and antimicrobial activity of some derivatives on the basis (7-hydroxy-2-oxo-2H-chromen-4-yl)-acetic acid hydrazide, Molecules 11 (2) (2006) 134–147, https://doi.org/10.3390/11010134.
[37] Z.H. Mahdi, T.A. Alsalim, H.A. Abdulhussein, A.A. Majed, S. Abbas, Synthesis, molecular docking, and anti-breast cancer study of 1-H-indol-3-carbohydrazide and their derivatives, Results. Chem. 11 (2024) 101762, https://doi.org/10.1016/j.rechem.2024.101762.
[38] M.K. Mohammed, Z. Al-Shuhaib, A.A. Al-Shawi, Synthesis, characterization and cytotoxicity appraisal of original 1, 2, 3-triazole derivatives, against breast cancer cell lines (MDA-MB-231), Mediterr. J. Chem. 9 (2019) 305–310, https://doi.org/10.13171/mjc941911161021mkm.
[39] N.M. Nasir, T.A. Alsalim, A.A. El-Arabey, M. Abdalla, Anticancer, antioxidant activities and molecular docking study of thiazolidine-4-one and thiadiazol derivatives, J. Biomol. Struct. Dyn. 41 (2023) 3976–3992, https://doi.org/10.1080/07391102.2022.2060306.
[40] J.A. Bell, Y. Cao, J.R. Gunn, T. Day, E. Gallicchio, Z. Zhou, R. Levy, R. Farid, PrimeX and the Schrödinger computational chemistry suite of programs, Int. Tables Crystallogr. 18 (2012) 534–538, https://doi.org/10.1107/97809553602060000864.
[41] H.P. Ebrahimi, J.S. Hadi, T.A. Alsalim, T.S. Ghali, Z. Bolandnazar, A novel series of thiosemicarbazone drugs: from synthesis to structure, Spectrochim. Acta A 137 (2015) 1067–1077, https://doi.org/10.1016/j.saa.2014.08.146.
[42] Z.Y. Kadhim, H.G.J. Alqaraghuli, Synthesis, docking study, and structural characterization of new bioactive thiazolidine-4-one derivatives as antibacterial and antioxidant agents, Russ. J. Bioorg. Chem. 51 (2025) 729–742, https://doi.org/10.1134/S1068162024605007.
[43] M. Koley, J. Han, V.A. Soloshonok, S. Mojumder, R. Javahershenas, A. Makarem, Latest developments in coumarin-based anticancer agents: mechanism of action and structure–activity relationship studies, RSC. Med. Chem. 15 (2024) 10–54, https://doi.org/10.1039/D3MD00511A.
[44] T. Ishikawa, M. Seto, H. Banno, Y. Kawakita, M. Oorui, T. Taniguchi, Y. Ohta, Design and synthesis of novel Human epidermal growth factor receptor 2 (HER2)/epidermal growth factor receptor (EGFR) dual inhibitors bearing a pyrrolo[3,2-d] pyrimidine scaffold, J. Med. Chem. 54 (2011) 8030–8050, https://doi.org/10.1021/jm2008634.